Flight Dynamics and Control Analysis for Motor Sizing and Failure Accommodation for a Lift+Cruise eVTOL Near Hover

David Hartman
Research Aerospace Engineer
Flight Dynamics Branch
NASA Langley Research Center
Hampton, VA, USA

George Altamirano
Research Aerospace Engineer
Flight Dynamics Branch
NASA Langley Research Center
Hampton, VA, USA

Peter Suh
Aerospace Engineer
Flight Controls & Dynamics Branch
NASA Armstrong Flight Research Center
Edwards, CA, USA

ABSTRACT

This paper demonstrates methods of aircraft sizing, flight dynamics modeling, and performance analysis using a lift+cruise concept vehicle with an electric powertrain and variable-speed rotors. The central focus is the development of methods to relate the aircraft design sizing constraints to achievable maneuverability and predicted handling qualities. A toolchain is demonstrated that performs aircraft sizing, mass moment of inertia estimation, powertrain modeling, trim optimization, dynamics linearization, handling qualities prediction, and quantification of achievable maneuverability under both nominal conditions and control effector failures. A convex optimization problem framework is introduced to compute agility bound estimates without requiring control system design or control allocation, potentially supporting rapid design iteration as well as early detection of deficiencies and undesirable operating conditions. This analysis is supplemented with more conventional methods of analysis to provide additional perspective and observations. Overall, the results suggest that each modeling and analysis element in the demonstrated toolchain adds significant value, with the combined approach supporting a more efficient and comprehensive exploration of trade-offs within the design space.

NOTATION

Electric Motor Modeling

b	Viscous damping coefficient ($\frac{\text{ft}\cdot\text{lb}\cdot\text{s}}{\text{rad}}$)
^{b}	Superscript indicating motor base condition
G_{inv}	Inverter voltage output gain
G_r	Gear ratio
I_q	Q-axis stator current (A, peak)
L_d	D-axis rotor self-inductance (H)
L_q	Q-axis rotor self-inductance (H)
M	Modulation ratio
^{nl}	Superscript indicating motor no-load condition
n_p	Number of pole pairs
P_L^p	Peak load power ($\frac{\text{ft}\cdot\text{lb}}{\text{s}}$)
^{r}	Superscript indicating motor rated condition
R_s	Stator resistance (Ohm)
V_b	Battery voltage at inverter terminal (V)
V_d	D-axis stator voltage (V, peak)
V_m	Motor design voltage (V)
V_q	Q-axis stator voltage (V, peak)
λ	Motor flux linkage (Wb)
τ_c	Coulomb friction loss (ft · lb)
τ_L	Motor torque load (ft · lb)
ω_m	Motor speed ($\frac{\text{rad}}{\text{s}}$)

Vehicle Dynamics Modeling

a	Amplitude of sinusoidal motion (rad/s)
A,B,C,D	Linear model matrices; subscript c indicates continuous time, otherwise discrete-time
$\mathbf{B}$	Control effectiveness mapping or matrix
I_x, I_y, I_z	Moment of inertia in body coordinates (slug · ft^2)
I_{xz}	Product of inertia in body coordinates (slug · ft^2)
m_{lin}, b_{lin}	Slope and intercept of linear model
n_{steps}	Number of discrete trajectory solution steps
p, q, r	Angular velocity states of aircraft (rad/s)
$r(t), r_i$	A reference trajectory, subscript for sample index
Δt	Time between discrete steps (s)
T_F	Total time for attitude tracking task (s)
u, x, y	Linear model input, state, output vectors
δ	Control inputs, subscript indicates name
m	Moment vector
ε	Allowable error fraction
ω	Frequency of sinusoidal motion (rad/s)
Ω, Φ	Allowable input and attainable moment subsets

Presented at the Vertical Flight Society's 81st Annual Forum & Technology Display, Virginia Beach, VA, USA, May 20–22, 2025.

INTRODUCTION

Background

Continuing advancements in electric vertical takeoff and landing (eVTOL) technology have led to the development of a variety of prototypes, progress towards certification (Ref. 1), and flight test demonstrations. Many eVTOL designs incorporate rotorcraft and fixed-wing vehicle characteristics to enable hover, transition, and forward flight modes. Various configurations have emerged including lift+cruise, tilt-wing, and tilt-rotor designs, with many of them integrating electric powertrains with advanced fly-by-wire control systems. A broad range of control effectors are utilized for these aircraft, including rotors with collective pitch, cyclic control, tilting mechanisms, and fixed-pitch with variable speed (i.e, "rpm-controlled"). While these new technologies offer attractive solutions to Urban Air Mobility (UAM) and Advanced Air Mobility (AAM) applications, they also present design challenges related to their performance, efficiency, and safety.

The availability of flight dynamics models offers many benefits to the conceptual design process. Take as an example a lift+cruise aircraft relying on fixed-pitch variable-speed rotors for hover maneuvering. If reasonably accurate models of the powertrain and flight dynamics are not available, it may be difficult to ensure the rotors will be supplied with enough power to generate adequate control responsiveness, especially if the aircraft must be able to continue flight following motor or actuator failures. Many eVTOL aircraft also possess redundant control effectors during some phases of flight, with designs incorporating various combinations of lifting rotors, tilting mechanisms, and trailing edge control surfaces. As a result of this added complexity, designers may need to consider advanced methods for control allocation to optimize power usage, maximize control authority and vehicle responsiveness, ensure safety, and maintain failure tolerance wherever possible. Addressing these interconnected systems at the conceptual design stage is an attractive strategy towards maximizing performance and ensuring the success of a particular eVTOL aircraft design.

A substantial portion of stability and control analysis often occurs later in the design process, such as during wind-tunnel testing or flight-testing phases. In the case for eVTOL aircraft, this is partially due to the challenges of developing accurate aerodynamic models for flight dynamics simulations. Additionally, eVTOL aircraft often possess redundant control effectors and utilize novel distributed electric propulsion (DEP) systems, motivating the development of new methods to analyze the relationship between aircraft sizing and achievable control system performance. To address these gaps, there have been numerous research efforts to improve sizing and performance analysis methodologies (Refs. 2–5) and aero-propulsive modeling capabilities that capture complex aerodynamic interactions (Refs. 6–11).

NASA has also engaged in research efforts to develop tools that enable rapid stability, control, and performance analysis. A physics-based modeling tool called SIMPLI-FLYD (Simplified Flight Dynamics for Conceptual Design) was presented by Lawrence et al. (Ref. 12) to assess flying qualities early in the design cycle. Further research was conducted to adapt methods from SIMPLI-FLYD to enable analysis of vehicles that utilize variable-speed motors (Refs. 13, 14) and assess electric motor power consumption (Refs. 15, 16). Recently, Malpica et al. (Ref. 17) demonstrated conceptual design exploration of an rpm-controlled hexacopter concept vehicle which included aircraft sizing, flight dynamics modeling, and analysis of pilot induced oscillation (PIO) prediction metrics. Selected methods and capabilities from these efforts are being integrated into an updated tool called FlightCODE (Flight dynamics and control modeling tools for COnceptual DEsign), and these include methods for uncertainty quantification (Ref. 18) and analysis of off-nominal conditions (Ref. 19). In addition to tool development, several piloted simulation campaigns have been conducted for quadcopter, hexacopter, and lift+cruise concept vehicles to validate predicted handling qualities metrics used in early design phases (Refs. 20, 21).

Preceding research efforts have demonstrated useful methodologies to relate eVTOL aircraft sizing with flying qualities analysis, and to develop aero-propulsive models for flight dynamics simulation. However, there remains a need for further development of these methods, particularly as they relate to aircraft with redundant control effectors subject to saturation and rate limitations. This research aims to enhance the capabilities of previously developed NASA aircraft sizing and flight dynamics modeling tools while also potentially reducing the need for time-consuming control system analysis during conceptual design.

Objectives

This paper presents a sizing and design suitability analysis of a turbo-electric lift+cruise concept vehicle, with a focus on the development and demonstration of tools and methods. The primary objectives were to identify connections between aircraft sizing conditions, trim selection, electric motor power limits, and achievable vehicle maneuverability. Beginning from a baseline configuration, design variants were generated by modifying a constraint in the sizing task to increase the power margin of the electric motors. Each design variant contains increasingly powerful motors that are used to control the speed of the lifting rotors. The analysis incorporates optimal control allocation for redundant control effectors and motor failure scenarios. Additionally, control system design and analysis was accomplished using existing rotorcraft flying qualities specifications.

The remainder of this paper is organized as follows. First, the baseline lift+cruise concept vehicle design is presented. Next, an approach to generate design variants is outlined, including an overview of the software and modeling methods used to compute optimal trim conditions, generate linear models, and calculate motor power limits. Following this is a description of the analysis techniques used for evaluating flight dynamics and control characteristics. The results section demonstrates an analysis of the design variants in hover conditions under nominal and motor failure scenarios. Lastly, the conclusion section summarizes the key findings.

BASELINE VEHICLE DESCRIPTION

The baseline conceptual vehicle for this research was the NASA-designed turbo-electric lift+cruise (Refs. 22,23). Renderings of the vehicle are shown in Figure 1. Rotor and motor numbering, rotational direction, and cant angle of the inboard rotors relative to the body-axes are also indicated.

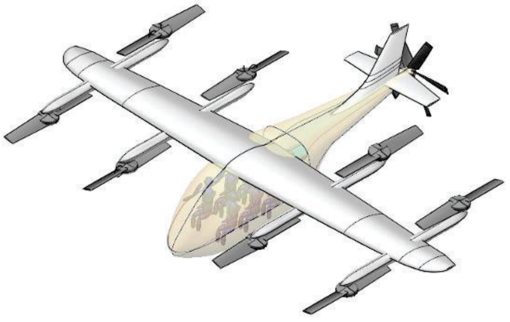

(a) Isometric view

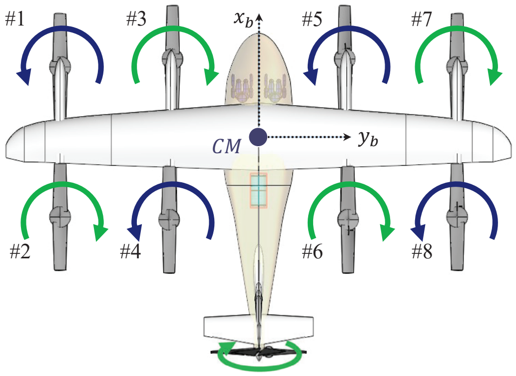

(b) Top view

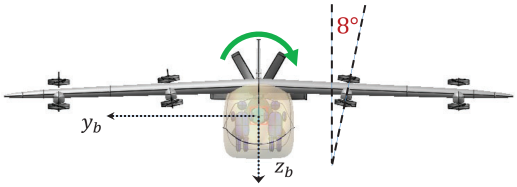

(c) Front view

Figure 1: Rendering of baseline lift+cruise vehicle.

This lift+cruise concept blends a fixed-wing airframe with eight variable-speed lifting rotors and a variable-pitch pusher propeller. In forward flight, the vehicle operates in an airplane mode which utilizes conventional trailing edge control surfaces including elevator, ailerons, and rudder for control. The four inboard motors are canted outwards by 8°, which is intended to help increase the achievable yaw moment. All lifting rotors are fixed-pitch, hingeless, and two-bladed. Each rotor has a dedicated electric motor connected to the rotor through a gearbox. Adjacent rotors rotate in opposite directions, which is intended to reduce coupling between attitude and heading control. The baseline rotor properties, main-wing and tail dimensions, and aircraft mass properties are listed in Table 1.

Table 1: Baseline lift+cruise design parameters.

Parameter	Value
Mass and Inertial Data	
Design gross weight	6,650 lb
I_x	11,060 slug · ft^2
I_y	11,530 slug · ft^2
I_z	20,300 slug · ft^2
I_{xz}	-1,800 slug · ft^2
Main Wing	
Span	48.3 ft
Chord	4.0 ft
Area	192.8 ft^2
Horizontal Tail	
Span	12.2 ft
Chord	2.8 ft
Area	34.6 ft^2
Vertical Tail	
Span	5.3 ft
Chord	4.5 ft
Area	23.9 ft^2
Lifting Rotors	
Number of rotors	8
Blades per rotor	2
Rotor radius	5 ft
Blade flap inertia	7.92 slug · ft^2
Blade twist	-15°
Blade pitch at 0.75R	16.5°
Chord taper ratio	0.75
Thrust-weighted chord	1.38 ft
Powertrain	
Peak power (per motor)	150 hp
Specification speed	8,000 rpm
Transmission gear ratio	7.62:1
Battery capacity	194 MJ

The original files containing design parameters are available on the NASA Systems Analysis and Concepts Directorate webpage (Ref. 24). The design is supplied as NASA Design and Analysis of Rotorcraft (NDARC) software (Ref. 25) files. For the work presented in this paper, version 1.18a of NDARC was used. Several minor modifications were made to the original aircraft design supplied in an NDARC ".list" file for the lift+cruise aircraft:

1. The cant angle defined for the inboard rotors was corrected for a typo that reversed the sign. The cant angle now matches the original design intent as illustrated in Figure 1(c).
2. Control connections to ailerons, elevator, rudder, flaps, and lifting-rotor speeds were revised to allow indepen-

dent articulation of these controls, allowing for more flexible trim optimization.

3. The main wing incidence angle was modified to +2°, and the horizontal stabilizer incidence angle was modified to -5°, improving cruise trim conditions.

The default control mixing applied for trimming in NDARC at hover conditions is given by Eq. 1, normalized for clarity to a per-column maximum of 1.

$$\begin{bmatrix} \omega_{m,1} \\ \omega_{m,2} \\ \omega_{m,3} \\ \omega_{m,4} \\ \omega_{m,5} \\ \omega_{m,6} \\ \omega_{m,7} \\ \omega_{m,8} \end{bmatrix} = \begin{bmatrix} 1 & 1 & -1 & 1 \\ 1 & 1 & 1 & -1 \\ 1 & 1/2 & -1 & -1 \\ 1 & 1/2 & 1 & 1 \\ 1 & -1/2 & -1 & 1 \\ 1 & -1/2 & 1 & -1 \\ 1 & -1 & -1 & -1 \\ 1 & -1 & 1 & 1 \end{bmatrix} \begin{bmatrix} \delta_{coll} \\ \delta_{latcyc} \\ \delta_{lngcyc} \\ \delta_{pedal} \end{bmatrix} \tag{1}$$

Note that in Eq. 1 the rank of the mixing matrix is 4, equal to the number of columns. One practical consequence of this is that there exist combinations of rotor speeds that cannot be generated using the available inputs if this mixing is enforced. Thus, avoiding enforcement of a fixed mixing strategy like Eq. 1 when optimizing trim conditions can increase flexibility, which might be especially important following failures.

DESIGN VARIANT SIZING AND MODELING

The process for generating the aircraft design variants with different powertrain sizes is illustrated in Figure 2. The required inputs are a set of initial design parameters and a sizing task. These serve as the starting point for a toolchain that supports aircraft sizing, trim optimization, and aircraft flight dynamics and powertrain performance modeling.

Aircraft Sizing

The inputs to NDARC were the initial aircraft design ".list" file and the accompanying sizing task ".run" file, which consists of a sizing mission and several sizing conditions. The sizing mission properties for each segment are summarized in Table 2, and the profile is illustrated in Figure 3. A complete description and development of the sizing mission can be found in Refs. 22, 23, and 26, with only selected highlights included here. The sizing mission requires two identical flights, each involving hover, transition, climb, cruise, and descent phases. Each of the climb and cruise phases are 37.5 nautical miles (nmi) in distance followed by a vertical descent and 30 second hover out of ground effect. An additional sizing requirement applied to the battery of the turboelectric drivetrain requires that the aircraft can cruise a distance of 20 nmi and hover for 3 min using solely battery power in the event of a turbine or generator failure. The mission profile is intended to represent required mission capability for notional UAM operations (Ref. 26). It does not explicitly target a guarantee of acceptable flying qualities, adequate motor torque margin for maneuvering, nor the feasibility of continued operations following the failure of one of the wing-mounted lifting rotors.

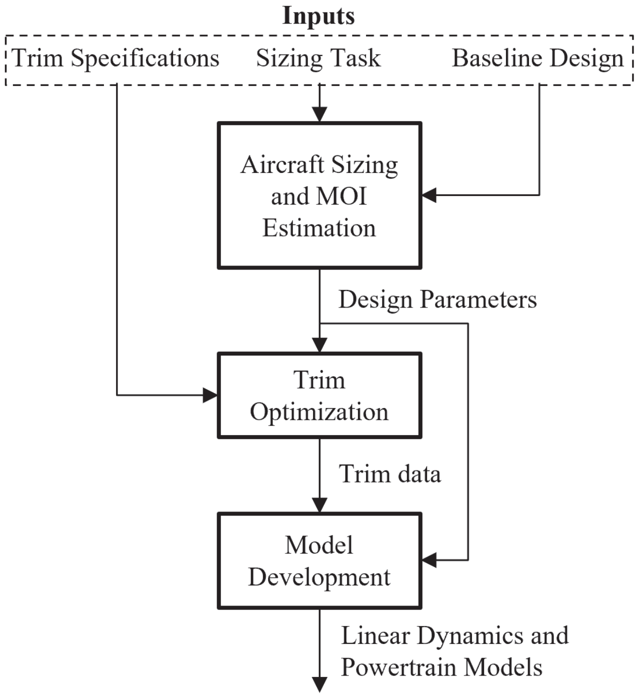

Figure 2: Process used to generate design variants and associated dynamic models.

To generate design variants with increased power margin on the lifting rotors and motors, an additional sizing condition was added to the original sizing task that required the vehicle to sustain a specified load factor along the body z-axis (n_z) while hovering at 6,000 ft International Standard Atmosphere (ISA) conditions. The load factor requirement started from the baseline design ($n_z = -1.00$ g), and varied in magnitude in increments of 0.05 g to $n_z = -1.75$ g, with an additional load factor design variant of $n_z = -1.77$ g included as the largest magnitude load factor for which the sizing task converged. This resulted in 17 unique design variants considered. The variants do not only differ by motor power; gross weight, wing area, fuel capacity, etc., all vary as required such that the vehicle design satisfies the original sizing mission plus the added load factor constraint. For the remainder of the paper the individual design variants are referred to by the load factor used to size them, with the $-n_z$ direction implied, e.g., "1.35 g design variant" would refer to the design satisfying $n_z = -1.35$ g.

Moment of Inertia Estimation

NDARC version 1.18a outputs aircraft mass moments of inertia (MOI) based on user-supplied radius of gyration values. However, the implementation requires these values to be fixed prior to sizing the aircraft, making it difficult to adequately capture the effect of the sizing mission on the vehicle's mass moment of inertia and radius of gyration values. Additionally,

Table 2: Sizing mission segments and properties.

Segments	1	2	3	4	5	6	7	8	9	10
Initial Alt. (MSL ISA)	6,000	6,000	6,050	6,050	10,000	6,050	6,050	6,050	6,000	10,000
Final Alt. (MSL ISA)	6,000	6,050	6,050	10,000	10,000	6,050	6,050	6,000	6,000	10,000
Time (s)	15	30	10	t_{climb}	t_{cruise}	10	30	30	15	1,200
Distance (nmi)	-	0	0	D_{climb}	37.5-D_{climb}	0	0	0	0	-
Speed	-	-	0	V_x	V_{br}	0	0	-	-	V_{be}
ROC (ft/min)	-	100	0	≥ 900	0	0	0	-100	-	0
% Power Available	10%	100%	100%	P_{climb}	P_{cruise}	100%	100%	100%	10%	P_{cruise}

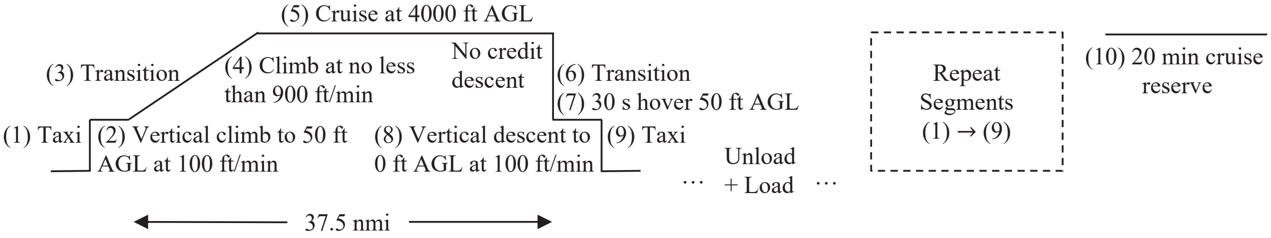

Figure 3: Sizing mission profile.

the current approach to MOI computation neglects off-axis terms in the inertia matrix that are sometimes relevant to the vehicle's flight dynamics characteristics. Because NDARC sizing missions rarely include conditions with nonzero angular velocity, accurate MOI values are often not required for NDARC's sizing calculations. However, the analysis of aircraft flight dynamics does require realistic mass MOI estimates, and ideally these MOI estimates should be driven directly by variations in the design's mass properties output by NDARC. To address this limitation, a tool was developed using The MathWorks® MATLAB® (Ref. 27) software to parse the NDARC aircraft design files for each variant and rapidly estimate the mass MOI. The estimation is constructed based on a component-wise analysis of the design, with user input specifying appropriate assumptions for each component type.

For the lift+cruise design considered here, these assumptions include modeling the wing-mounted motors and transmissions as point masses, the fuselage as a cylinder, and the wing and tail surfaces as cuboids. The geometry information describing component locations and dimensions required for MOI estimation were derived directly from the NDARC output files, with limited exceptions including the turboshaft engine and transmission. Locations for these components were not defined in the NDARC output files and were based on existing conceptual drawings of the vehicle. Due to the assumptions and limitations of this MOI estimation approach, the resulting mass MOI values are expected to be somewhat lower than would be found using a more accurate estimation method that included detailed geometry and component densities. Nevertheless, this approach does capture the trend of increasing radius of gyration with increased weight of the wing-mounted motors. A comparison of an MOI estimate generated using this method against a more comprehensive estimate using OpenVSP showed about a 10% difference. This is significantly more accurate than the values obtained using the original fixed radius of gyration values, and was judged to be sufficient for the purposes of this analysis.

Trim Optimization

The trim solving capabilities built into NDARC version 1.18a require the user to specify a mixing scheme or fix any excess trim variables. This presents difficulties when studying the performance of aircraft with redundant control effectors. For example, when trimming during an approach at a given airspeed and glidepath angle, a lift+cruise aircraft could potentially utilize pitch and roll attitude, flaps, elevator, aileron, rudder, pusher collective and speed, and the speed of all eight lifting rotors. Choosing an appropriate trim strategy in NDARC for these situations is challenging, and poor selection of the control mixing matrix or the fixed values of component controls could negatively influence an assessment of the design's suitability. It is especially difficult to analyze the feasibility of flight following an actuator failure without a means to select a trim condition according to some sensible optimality criteria. In these cases, the feasible trim space is challenging to explore without more sophisticated trimming tools, and detailed analysis might require large scale one-factor-at-a-time sweeps of the available trim variables.

MANITO (MATLAB and NDARC Iterative Trim Optimizer) was designed as a prototype tool to partially fill this gap. MANITO operates in the MATLAB environment and relies on the constrained nonlinear optimization solver `fmincon` to iteratively trim NDARC to an optimal solution. This is accomplished in part by utilizing an option that instructs NDARC not to attempt to trim the aircraft controls, and instead only to compute aircraft performance at the specified flight condition. Currently, MANITO cannot be used during a sizing task in NDARC, so initial design sizing must still be performed using NDARC's built-in trim capabilities. However, once an aircraft design file has been generated, MANITO can be used to compute optimal trim solutions based on the user's specifications, constraints, and objective function. The program is designed to handle nonlinear constraints on any combination of trim variables or performance values, and accepts user-defined nonlinear cost functions that can be a function of trim variables (e.g., rotor speed, pitch attitude, etc.) or performance values reported by NDARC (e.g., total power consumption).

In this application, MANITO was instructed to constrain linear and angular accelerations to zero, to respect known bounds on selected trim variables where appropriate, and provided with a cost function intended to select for a desirable trim condition within the space of possible solutions. Starting from an initial guess, MANITO provides an interface for `fmincon` to iteratively call NDARC efficiently. Each candidate solution is processed by MANITO into an NDARC input file along with the perturbations in each trim variable that are required to form an estimate of the local partial derivatives using central-differences. During each iteration of the optimization, the output from a single NDARC call is used to extract all of the required derivatives, costs, and constraint values, and these are supplied to `fmincon` for it to compute the next candidate optimal solution. When the solver reaches a trim value that satisfies the constraints and optimality criteria, the solution is saved along with the NDARC output files that were generated.

Linear Dynamics Models

Dynamic models of aircraft performance suitable for handling qualities prediction or control design evaluation cannot be directly produced by NDARC version 1.18a. For these applications, external tools must be used. FlightCODE is a tool for generating linear models based on NDARC outputs. For a given aircraft design file and trim solution file, FlightCODE generates a linear model representing the dynamics about the supplied trim condition. FlightCODE cannot compute trim solutions internally. The pre-release version of FlightCODE that was used to generate the models in this paper includes, for each rotor: a rotor speed state (i.e., rpm), three-state inflow dynamics based on Peters-HaQuang formulation (Ref. 28), and a six-state second-order blade flapping model. Thus, in addition to the aircraft's nine six-degrees-of-freedom (6DOF) rigid-body states for velocity, angular velocity, and orientation (roll, pitch, and yaw), each rotor has ten dynamic states associated with it.

The "full-order" model generated by FlightCODE is then reduced using balanced reduction techniques based on Hankel singular values. This requires careful selection of appropriate inputs and outputs. For this study focused on the evaluation of hover conditions, motor torques were the inputs to the model, and the rigid-body velocity, angular velocity, attitude, heading, and rotor speed states were chosen as outputs. Given these selections, the linear models retained sufficient accuracy with $n_{6\text{DOF}} + n_{\text{rotors}}$ states, which for flight conditions with no failed motors and the pusher-prop inactive resulted in 17 retained states. In the case of a single failed motor the number of inputs, outputs, and states were all reduced by one.

Calculation of Electric Motor and Battery Limits

A sized vehicle's motor specification speed, maximum rated power (MRP), maximum continuous power (MCP), peak torque, and a power limit defined from peak torque at the specification speed are all output by NDARCp. Given this information, motor limits which may affect vehicle and control performance can be derived. An overview of these motor limits is provided in this section. Further details on powertrain sizing, verification and validation are reported in Ref. 29. A conceptual motor torque-speed map depicting motor limitations in both speed and torque load is provided in Figure 4.

Sustained motor torque in the Intermittent Operations region of the conceptual motor map leads to motor component temperatures increasing beyond the motor temperature rating, which may reduce reliability over time. Therefore, a useful practice is to size motors so that they primarily operate within the Continuous Operations region of the motor map. Another useful practice is to size motors so they do not undergo significant decrease in torque capability from the effect of back-electromotive force (EMF). The reduction in peak torque load starting at the base speed in Figure 4 is consistent with certain motor manufacturer datasheets.

For improved handling qualities (see Ref. 17), it was determined that the motor map development process should allow for a motor map extension (see Figure 4). As an example, the peak torque may be extended to the right with a higher battery voltage than the motor's rated voltage. Further extensions of the map require inverter flux weakening (FW) technology (Ref. 30) to reduce the effect of back-EMF. Motor map extensions using inverter FW technology may also result in a decrease in peak torque capabilities to maintain constant power.

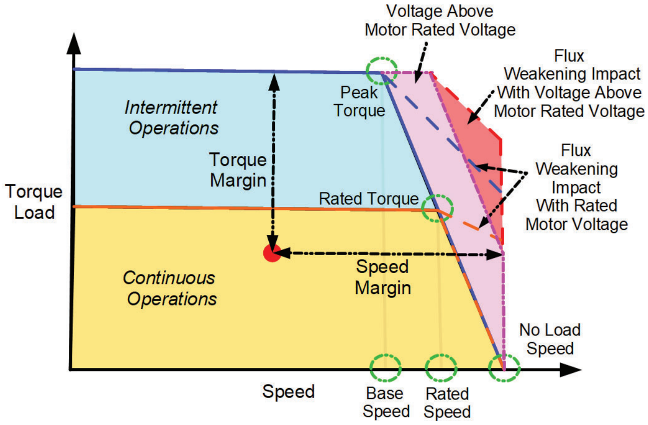

Figure 4: Conceptual motor torque-speed map.

At the motor's rated DC voltage, the peak torque in Figure 4 was assumed to be achieved at the motor base speed. The MRP was defined at the intersection of the peak torque and base speed. The MCP was defined at the highest speed which coincided with the maximum continuous torque (MCT). Manufacturers may rate their motors at a speed and torque where efficiency is optimal. Here, it was assumed that the motor rated speed and NDARC specification speed coincide. It was also assumed that the motor rated torque and MCT coincide.

The direct quadrature (DQ) frame (Ref. 31) is a rotating reference frame, which is used to transform alternating current (AC) motor three-phase currents and voltages into direct current (DC)-like components aligned with the motor rotor. The DQ frame is used to analyze and develop control laws for pulse magnet synchronous motors (PMSMs) and brushless direct current (BLDC) motors. In this paper, the DQ frame was used to approximate realistic motor limits which could impact vehicle sizing.

The DC voltage, necessary for motor rated and peak torque-speeds, are typically provided in a motor datasheet. The PMSM voltage constraint equation, necessary to derive how much higher the speeds can be increased for a given torque load and DC voltage was defined from the inverter voltage constraint as

$$G_{inv} V_b \geq \sqrt{\left(R_s^r I_q^r + \lambda^r n_p \omega_m^r\right)^2 + \left(-L_q^r I_q^r n_p \omega_m^r\right)^2} \tag{2}$$

where G_{inv} is the inverter gain, R_s, is stator resistance, I_q is Q-axis current, λ is flux linkage, n_p, is number of pole pairs, ω_m, is motor speed, and L_q is Q-axis inductance. The voltage constraint in Eq. 2 was crucial to producing the motor map in Figure 4. The superscript r indicates the value refers to the motor's rated continuous operating condition.

Equation 2 may be rearranged to determine motor peak speed for any given load torque. These values determine the baseline motor continuous and intermittent performance without FW control, as shown in Figure 4. The peak motor speed in the Intermittent Operations region of Figure 4 is given in Eq. 3.

$$\omega_m^p = \frac{-R_s I_q \lambda + \sqrt{G_{inv}^2 V_b^2 (\lambda^2 + L_q^2 I_q^2) - L_q^2 I_q^2 R_s^2 I_q^2}}{n_p (\lambda^2 + L_q^2 I_q^2)} \tag{3}$$

Equation 3 is applicable for any given DC voltage in the absence of FW control. The current may be computed for any known torque loads on the PMSM as

$$I_q = \frac{2}{3} \frac{(\tau_L + \tau_c + B\omega_m^p)}{\lambda n_p} \tag{4}$$

where τ_L is the torque load, τ_c is Coulomb torque, and B is the dynamic viscous torque coefficient. The rated motor constants can be substituted into Eq. 3 to calculate peak speed. Because current is a function of speed, Eqs. 3 and 4 can be solved iteratively for ω_m^p.

The base speed of the motor (ω_m^b) is achievable assuming the availability of the rated DC voltage at the peak power condition. The base speed was computed by NDARC as

$$\omega_m^b = G_r \frac{P_L^p}{\tau_L^b} \tag{5}$$

where τ_L^b is the peak torque at the base speed and P_L^p is peak load power, or what NDARC defines as MRP. The base speed (see Figure 4) may additionally be computed by substituting peak current, I_q^p, defined as in Eq. 6, as well as the motor's rated DC voltage, V_m^r, into Eq. 3.

$$I_q^p = \frac{2}{3\lambda n_p} \left(\frac{P_L^p}{\omega_m^b} + \tau_c + B\omega_m^b \right) \tag{6}$$

The no-load speed (NLS) is computed by substituting no-load current, I_q^{nl}, defined in Eq. 7, as well as the motor's rated DC voltage, V_m^r, into Eq. 3 and solving the implicit relation.

$$I_q^{nl} = \frac{2}{3\lambda n_p} \left(\tau_c + B\omega_m^b \right) \tag{7}$$

The motor NLS (ω_m^{nl}) was assumed to be the maximum motor speed for this work. Exceeding the no-load speed with a significant torque load—while theoretically possible with a larger voltage source and/or FW control—may lead to mechanical damage of the motor.

The peak load torque driven at any condition depends on the speed of the motor. Equation 2 was solved for peak load torque as a function of motor speed. The physical solution of the resulting quadratic equation solved for peak load torque was derived as

$$\begin{aligned} \tau_L^p = & -\tau_c - B\omega_m - \\ & \frac{3\lambda n_p \left(R_s \lambda \omega_m - \sqrt{G_{inv}^2 V_b^2 (R_s^2 + L_q^2 n_p^2 \omega_m^2) - L_q^2 n_p^4 \omega_m^4 \lambda^2} \right)}{2\left(R_s^2 + L_q^2 n_p^2 \omega_m^2\right)} \\ & \tau_L^p < \tau_L^b \\ & \omega_m^{nl} \geq \omega_m \geq \omega_m^b \end{aligned} \tag{8}$$

The peak load torque, τ_L^p, computed by Eq. 8 is applicable between the base speed and motor NLS when the motor's rated DC voltage is assumed to be available to the inverter.

The combination of a battery with higher voltage than the motor's rated voltage and inverter FW control technology affects the peak torque calculation. The results reported in this paper assume both of these powertrain enhancements were available for motor map extension. With DC voltage exceeding motor rated voltage, the peak torque may be held constant between the base speed and rated speed (see Figure 4). Assuming the availability of both inverter FW control and a higher voltage battery, power may be assumed to be held constant from the intersection of the peak torque and rated speed in Figure 4. These voltage and FW control enhancements affect peak torque calculation, here defined as in Eq. 9.

$$\tau_L^P \triangleq \begin{cases} \tau_L^b & \omega_m \leq \omega_m^r \\ \frac{\omega_m^r \tau_L^b}{\omega_m} & \omega_m^r < \omega_m < \omega_m^{nl} \end{cases} \tag{9}$$

To allow the motor to drive the peak load torque at the rated speed as observed in Figure 4 the DC battery voltage was computed using Eq. 10.

$$V_m^p = \frac{1}{G_{\text{inv}}} \left[n_p \left(\lambda^2 + \left(L_d I_q^p \right)^2 \right) \right] \omega_m^r \tag{10}$$

To extend continuous motor operations beyond the rated speed using inverter FW control, a constant power relationship was also assumed up to the motor NLS beginning from the intersection of the MCT at the rated speed. This assumed power relationship to the right of the rated condition for continuous operations was not assumed to be invalidated or changed by the increase in DC voltage so as not to cause thermal protection issues. The peak speed assuming available inverter FW control and battery voltage as computed from Eq. 10, was defined as in Eq. 11.

$$\omega_m^p \triangleq \frac{\omega_m^r \tau_L^b}{\tau_L} \leq \omega_m^{nl} \tag{11}$$

MANEUVERABILITY ANALYSIS METHODS

The flight dynamics and control characteristics of the aircraft designs were analyzed in two phases. The first phase of analysis utilizes convex optimization methods to quantify the achievable agility of each design given actuator saturation and rate limits. This analysis is intended to help identify and eliminate deficient designs and perform meaningful trade studies, without requiring a detailed control design effort or extensive simulations. The second portion of the analysis selects a subset of the design variants and synthesizes a control system to target desirable performance based on existing rotorcraft flying qualities specifications (Refs. 32,33) and stability requirements (Ref. 34).

Background and Existing Methods

Estimating the feasible maneuvering performance of a vehicle design concept with redundant control effectors presents several challenges, especially when considering off-nominal scenarios such as actuator failures. If trim conditions can be found within the feasible operating limits of the aircraft, and if linear models can be constructed to represent the dynamics of the aircraft near these trims, the predicted handling qualities of a design can be explored. However, this typically requires the development of a control allocation strategy for the vehicle in combination with implementation of a command-tracking feedback control system. A disadvantage of this approach is that it combines the performance of the vehicle with the performance of the control system, which can leave uncertainty about the true bounds on feasible maneuverability of the design and make it more difficult to establish the root cause of any noted deficiencies. More broadly, control system design requires substantial subject matter expertise and time investment, especially when complex operating conditions and off-nominal or failure scenarios are considered. Further challenges arise in part due to the impact of various actuator constraints, which can create nonlinear behaviors requiring special attention for a successful control design. Thus, while closed-loop performance analysis and control system design studies can be an important phase of an aircraft sizing and development process, there are significant motivations to explore ways to address some of these questions in an efficient way without resorting to the implementation of a control system.

There is substantial literature describing attainable moment subset (AMS) applications in the context of control allocation (see Ref. 35). These methods have also been leveraged to support handling qualities prediction for aircraft sizing, without requiring the design of a feedback control system. For example, Ref. 4 utilizes an AMS analysis for aircraft sizing and handling qualities prediction, drawing a connection between an estimated AMS and a proposed required moment subset (RMS) that needs to be attainable for acceptable predicted handling qualities to be feasible. Typically, an AMS analysis defines constraints on controllable inputs to the vehicle such that the n_u control inputs ($u \in \mathbb{R}^{n_u}$) remain constrained within a specified set $\Omega \in \mathbb{R}^3$. A mapping ($\mathbf{B}$) from control inputs (u) to a vehicle moment vector (m) is also modeled, such that in the linear case a control effectiveness matrix $\mathbf{B}$ is constructed such that $m = \mathbf{B}u$. Such a mapping produces an image (Φ, the AMS) of the constrained input subset Ω that is attainable through the control effectiveness mapping, i.e., $\mathbf{B}(\Omega) \to \Phi$. In the context of aircraft design, this AMS (Φ) might be assessed using various measures of adequacy in order to improve confidence that a vehicle design can feasibly satisfy maneuverability requirements.

A potential challenge of using this approach might lie in constructing an appropriate mapping $\mathbf{B}(\Omega) \to \Phi$. If the analysis is chiefly concerned with evaluating Φ under control effector inputs that permit a linear mapping $m = \mathbf{B}u$, then Φ is described by a convex hull and provides the moment (or angular acceleration) response of the aircraft to all control positions in Ω. Any moment lying within the resulting convex hull Φ is then guaranteed to be feasible under these assumptions. If there are internal states such as actuator dynamics or rotor speeds that are influenced by the control inputs and contribute to the generated moment, forming a linear control effectiveness matrix $\mathbf{B}$ for this purpose may introduce some subtleties that should be carefully considered. For example, in some cases it might be appropriate to form $\mathbf{B}$ using a zero-order hold on the inputs over a time-period of interest to discretize the aircraft's dynamics. However, the handling of various state constraints (such as actuator rates, motor speed limits, etc.) may require special attention to ensure the limits are respected and the results interpreted appropriately. Similarly, the implications of known nonlinearities or assumed instantaneously-reached equilibria in the mapping $\mathbf{B}(\Omega) \to \Phi$ should be considered when estimating or interpreting Φ in the context of handling qualities.

Convex Optimization

Convex optimization problems require that both the objective function and the set over which the objective must be optimized satisfy certain convexity requirements. When suitable, a convex optimization formulation of a problem can offer many advantages over more general non-convex approaches. These include the ability for convex optimization solvers to provide reliable indications of problem infeasibility if no solution exist, and to solve feasible problems very rapidly and reliably in comparison with more general non-convex solvers (Ref. 36). In this paper, convex optimization methods are used to estimate upper limits on the feasible maneuvering performance of a vehicle design without requiring the design of a feedback control system or control allocation strategy. This approach is based on the observation that given a discrete-time linear model with an appropriate cost function and state, input, and output limitations, it is possible to pose and efficiently solve a convex optimization problem to produce an optimal trajectory. By formulating the problem such that the optimal solutions reveal useful information about the performance capabilities of the aircraft, information relevant to aircraft sizing and predicted handling qualities can be obtained.

For the present application, convex optimization problems were posed and solved by leveraging CVXPY (Refs. 37, 38) and the convex optimization solver Clarabel (Ref. 39). CVXPY is an open-source program that allows convex optimization problems to be modeled within an extension of the Python language. CVXPY allows the user to avoid having to explicitly structure the problem into the standard form required by the convex solver, making the process of problem formulation and results interpretation much more intuitive and convenient.

Two distinct convex optimization problem formulations are proposed in this paper to analyze the feasible agility of an aircraft design. The first computes the maximum achievable amplitude of sinusoidal angular velocity at a specified frequency while maintaining a fully periodic state trajectory. This problem is intended to support the estimation of maximum feasible angular velocity along an arbitrarily chosen directional axis, and can help to identify directions of motion in which the aircraft may have limited maneuverability while also allowing quantification of trade-offs associated with design variants, operating conditions, or failure scenarios. Sinusoidal periodic trajectories are utilized for two reasons. First, incorporating frequency dependence potentially allows for a more structured view of how feasible motion changes as a function of the required frequency. Second, these trajectories are naturally bidirectional (i.e., the sinusoidal reference is zero-mean with equal amplitude in both positive and negative directions), and the requirement of full state-vector periodicity means that the maneuver could be continuously repeated, ensuring that all of the vehicle states and inputs remain bounded.

The second type of problem considered is a step-input attitude tracking task with quadratic cost on the attitude error. This optimization problem is intended to support estimation of the maximum feasible performance attainable during a moderate-amplitude pitch, roll, or yaw attitude response criteria maneuver as described in (Refs. 32,33). Importantly, the formulation allows the estimate to be obtained without any feedback control design, gain selection, or control allocation, potentially saving time and effort by allowing deficient designs, problematic operating conditions, and unrecoverable failure scenarios to be identified more quickly.

Maximum Amplitude Sinusoidal Angular Velocity The following problem is proposed: Let the continuous-time dynamics of a linear model of the system about a trim condition be represented as Eq. 12.

$$\begin{aligned} \dot{x}(t) &= A_c x(t) + B_c u(t) \\ \dot{y}(t) &= C_c x(t) + D_c u(t) \end{aligned} \tag{12}$$

Here, the $x(t) \in \mathbb{R}^{n_x}$ is the state vector, $u(t) \in \mathbb{R}^{n_u}$ is the input vector, and $y(t) \in \mathbb{R}^{n_y}$ is the output vector, all continuous functions of time (t), and the matrices A_c, B_c, C_c, and D_c are constant matrices of appropriate size. In this application, rotor shaft torque is included in $u(t)$, and the corresponding rotor speeds are included in $x(t)$.

Assume a desired trajectory $ar(t)$ for a given state of the system, $x_{track}(t)$, can be represented as a sinusoid with frequency ω as in Eq. 13, with a remaining an undetermined amplitude for now.

$$ar(t) = a \sin(\omega t) \tag{13}$$

For a given angular frequency ω, the dynamics expressed in Eq. 12 are discretized using a zero-order hold on the system input. Let the corresponding interval be given as Eq. 14.

$$\Delta t = \frac{2\pi}{\omega n_{steps}} \tag{14}$$

The integer n_{steps} will represent the number of discrete input vectors u_i to include in the optimization problem, and the number of discrete state vectors x_i will be $n_{steps} + 1$. To adequately capture the feasible motion of the vehicle at the selected frequency over a single period, $n_{steps} = 40$ was used for this analysis. This value worked acceptably well for the systems under consideration here. In general, the value of n_{steps} should be considered carefully to ensure meaningful results are obtained. A smaller number of steps reduces the dimensionality of the optimization problem, and might be necessary for systems with a very large number of states or inputs. If a known frequency is expected to be used for control signal updates, it might be appropriate to use it as a lower bound on Δt in order to enforce a limit on how finely the input to the system can be varied. Conversely, too small a value of n_{steps} could limit the resolution of the optimization and result in poor approximation of the feasible motion limits of the vehicle design. Thus, this value may need to be adjusted based on the system dynamics and frequency ω of desired motion.

The system is discretized with the selected step size Δt, assuming a zero-order hold on the inputs such that the discrete-time system is given in Eqs. 15.

$$\begin{aligned} A &= e^{\Delta t A_c} & B &= \left(\int_0^{\Delta t} e^{\tau A_c} \, d\tau \right) B_c \\ C &= C_c & D &= D_c \end{aligned} \tag{15}$$

The discrete-time linear model is now given by Eqs. 16.

$$\begin{aligned} x_{i+1} &= A x_i + B u_i \\ y_i &= C x_i + D u_i \end{aligned} \tag{16}$$

For convex optimization, this state-update equation is treated as an equality constraint enforced at each time index i. The rotor speed state constraints for the k-th rotor can be enforced as the inequalities shown in Eq. 17.

$$0 \le \left(x_{k,i} + x_k^*\right) \le \bar{x}_k \tag{17}$$

Where x_k^* represents the k-th rotor's trim speed, and $\bar{x}_k$ represents the maximum speed achievable for that rotor given the motor's NLS speed converted into an equivalent rotor speed limit based on the transmission gear ratio. Similarly, the rotor torque constraints can be modeled by the inequalities shown in Eq. 18.

$$0 \le \left(u_{k,i} + u_k^*\right) \le \min\left(m_{lin}\left(x_{k,i} + x_k^*\right) + b_{lin}, \bar{u}_k\right) \tag{18}$$

Here, the linear model parameters m_{lin} and b_{lin} are selected to represent a linear fit of the peak torque limit when operating above the rated speed (see Figure 4), with $\bar{u}_k$ representing the torque limit when operating below this speed. Note that the upper limit defined by the right side of Eq. 18 provides an upper bound on rotor torque and is required to be a piecewise concave function of $x_{k,i}$, which is only an approximation of the torque limitation in this region but can serve as a more accurate boundary than simply assuming a constant upper limit for torque. It is not strictly necessary that the lower torque limit be zero, but for this application it was expected that the motors may not be capable of generating significant braking torque.

The vehicle must track is a prescribed periodic angular velocity. To ensure the full state trajectory of the vehicle remains periodic, enforce the constraint given by Eq. 19.

$$x_0 = x_{n_{steps}} \tag{19}$$

This requires that the final state of the trajectory (for which no control input is computed) will be identical to the starting state of the trajectory (which will have a computed optimal control input). Note that for this problem there is no enforcement of an initial condition for the state vector. Instead, the convex optimization is allowed to compute the optimal periodic trajectory for all internal states so long as Eq. 19 is satisfied. The model used for this analysis includes aircraft position and heading states in the state vector to ensure that the optimal solution does not allow for unbounded changes in the vehicle position or heading, which otherwise might be permitted under the other constraints if these states were omitted and additional conditions were not added.

The targeted motion for this analysis is a sinusoidal variation in angular velocity in a specified direction. Given a unit vector representing the direction of desired angular velocity, a state transformation is computed and applied such that the specified angular velocity states are transformed from body-fixed axes into a control coordinate system (C), with the x-axis of this new coordinate system aligned with the desired motion direction. The trajectory tracking constraint can then be expressed as the inequality shown as Eq. 20.

$$\left|ar_i - x_{k_{track},i}\right| \le a\varepsilon_{track} \tag{20}$$

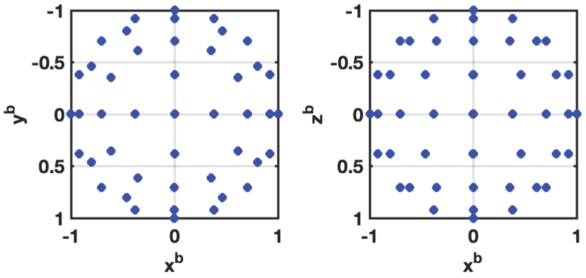

Figure 5: 2D views of the unit vector sphere used for sampling angular motion, top-down view on left, right-side view on right.

Where $r_i = \sin\left(\omega i \Delta t\right)$ represents the value of the sinusoid at time $i\Delta t$, ε_{track} is an allowable tracking error expressed as a fraction of the sinusoid amplitude a, and a is the sinusoid amplitude that will be maximized by the convex optimization given the other problem constraints. Because the only optimization objective given is to maximize a, full authority of the control inputs will typically be utilized to achieve this objective, and there are no gains or costs that must be selected or tuned. For this analysis $\varepsilon_{track} = 2\%$ was used.

Off-axis error is defined to limit motion along the y and z axes in the C coordinate system, and is constrained via the inequality given as Eq. 21.

$$\left\|x_{k_{off-axis},i}\right\|_2 \le a\varepsilon_{off-axis} \tag{21}$$

Here, the subscript $k_{off-axis}$ indicates the states of x_i corresponding to the two (y and z) off-axis motion states, and $\varepsilon_{off-axis}$ is a selected fraction of the amplitude a. For this analysis, $\varepsilon_{off-axis} = 10\%$ was used, meaning that 10% of the on-axis amplitude was the maximum allowed 2-norm of the off-axis angular velocity for each discrete-time index i.

This formulation allows for the direction of desired angular motion to be arbitrarily defined. For example, angular velocity in the roll (p), pitch (q), or yaw (r) directions are generally of interest. However, establishing the feasible periodic angular velocity about other axes is also useful for forming a more complete picture of the vehicle's feasible maneuvering envelope, particularly in the presence of asymmetric control effector failures. To sample the space of possible motion directions, a selection of unit vectors is constructed from a unit sphere. These selections are made such that principal directions (x, y, and z) are included, and symmetry of sampling across the x-y, x-z, and y-z planes is achieved. The selections used for this paper are shown in Figure 5.

This selection produces 74 unique unit vectors, with spacing of points in the x-y plane at z=0 of 22.5°, and spacing of points in the x-z plane at y=0 of 22.5°. Due to the symmetries described and the periodic angular velocity problem posed, the maximum feasible sinusoidal tracking amplitude solution for a given direction will be identical to the solution obtained for the negative of that direction. This property might be called "point symmetry" or "central symmetry." To illustrate, consider that a solution computed for a direction representing pitch oscillation with desired direction of angular velocity in the body-fixed coordinate system of $[0,1,0]$ will be identical to one computed for $[0,-1,0]$ with a phase shift of 180°. Thus, it is possible to reduce the number of unique directions for which a solution is computed to eliminate these redundancies, which results in 37 unique directions.

After computing the maximum amplitude a of motion in each direction, it may also be of interest to compute the "volume" of the total feasible motion. This provides a single quantitative measurement of feasible motion capability, which may be useful for comparing the relative maneuverability of design variants, and measuring the impact of various failure scenarios. To support this interpretation of the data, points on the unit sphere representing directions for which results are to be computed are connected into triangular faces using the MATLAB (`convexHull`) function, which is appropriate given the unit-vector spherical sampling approach being used. The mapping of triangular faces to individual vertices is then preserved through a deformation of this sphere, which is accomplished by multiplying the unit vectors describing each desired motion direction by the corresponding maximum feasible sinusoidal motion amplitude computed via convex optimization. A total volume is then calculated over this deformed sphere by summing the volumes of each tetrahedron formed by the unit vectors comprising these faces and the origin. Specifically, the total volume for each frequency is computed as in Eq. 22.

$$V_{tetrahedra} = \sum_{face_i}^{n_{faces}} \frac{1}{6} |v_1 \cdot (v_2 \times v_3)| \tag{22}$$

Each face includes three vertices from the original sampled unit sphere before deformation, and the vectors v_i represent the corresponding unit vectors after being scaled via their corresponding maximum amplitude. This approach avoids the assumption that the deformed sphere represents a convex hull, and is more direct than a general point-cloud bounding method such as the alphaShape function in MATLAB, which may require parameter tuning and careful analysis to produce the intended results. However, it is important to recognize that the problem formulation only guarantees feasibility of sinusoidal motion up to the computed maximum amplitude along the actual direction of prescribed motion. The analysis cannot guarantee feasibility of motion along axes other than those for which a solution is computed. Thus, the volume computed by Eq. 22, and the assumed triangular face boundaries on which it is based, should only be interpreted as estimates. Modification of the directions for which the convex optimization is performed will result in changes to the computed volume and may reveal or conceal maneuverability features.

The volume calculated in Eq. 22 is a function of frequency, and can be computed separately for each design variant, failure scenario, or unique trim condition of interest, potentially offering a meaningful quantification of feasible maneuverability. For this paper, the following conditions were analyzed:

- Hover conditions (5): Nominal (no failures), Motor 1 failed, Motor 2 failed, Motor 3 failed, Motor 4 failed.
- Design variants (17): Baseline through 1.77 g load factor.
- Direction of angular velocity (37): see Figure 5.
- Frequency of sinusoidal angular velocity (10): logarithmically spaced frequencies between 1 rad/s and 10 rad/s.

In total, this leads to 31,450 periodic trajectories generated using convex optimization as described in this section.

Moderate-Amplitude Attitude Changes Beginning from Eq. 12, consider a discretization of the dynamics via a zero-order hold assumption (Eq. 15) with a fixed number of time increments (n_{step}) and fixed total time (T_F). For this application, pitch and roll motion were assessed using $T_F = 5$ seconds, and yaw motion with $T_F = 10$ seconds, with $n_{step} = 100$, and $\Delta t = T_F / n_{step}$ for each. These values were found to produce acceptable results for the aircraft dynamics and conditions under consideration, and the magnitude of the attitude changes required. However, it is anticipated that variations in T_F and n_{step} will be required depending on the system's dynamics, the amplitude of the attitude change considered, and other factors.

The rotor torque inputs (u_k) and rotor speed states (x_k) remain constrained as previously described in Eqs. 17 and 18. The difference equation for the system given by Eq. 16 is again enforced as an equality constraint applied to each discrete step of the system. Other constraints applied to the state vector include an initial condition at the origin (i.e., $x_0 = 0$, the linear model's trim condition), and a final state constraint enforcing that at $x_{n_{step}}$, the angular rates are all zero, altitude is zero, the on-axis target attitude has been exactly achieved, and the 2-norm of the off-axis attitude angles are less than 10% of the on-axis desired attitude change, similar to the constraint enforced in Eq. 21.

The target attitude change ($r_{attitude}$) of the vehicle was varied in increments of 5°, with the cost to be minimized by the optimal trajectory chosen as Eq. 23.

$$\text{Cost} = \sum_{i=0}^{n_{steps}} \left(x_{k_{track},i} - r_{attitude}\right)^2 \tag{23}$$

This is simply a quadratic cost on the tracking error of the specified Euler angle state ($x_{k_{track}}$) and the desired attitude angle $r_{attitude}$. In general, the trajectory generated by this optimization might differ depending on the direction (i.e., sign) of the desired attitude angle due to asymmetric trim conditions and asymmetries in the way actuator limits influence the maneuvering limitations of the aircraft. Thus, for some applications it may be appropriate to compute results for both positive and negative values of $r_{attitude}$. It is worth emphasizing that no other costs are assigned in this analysis either to the inputs, states, or outputs of the model. Thus, full authority of the control inputs will be utilized to minimize this cost, subject to the constraints previously described. An advantage of this approach is that it avoids any need to tune the response characteristics via adjustments to weighting applied to the inputs or states.

RESULTS AND ANALYSIS OF LIFT+CRUISE DESIGN VARIANTS

Aircraft Mass Properties

Each of the design variants were analyzed in hover for nominal operating conditions and individual motor failures. Throughout this section, all models and subsequent performance data represent a gross weight consistent with 6 passengers, full fuel, no ground effect, and with atmospheric conditions of 6,000 feet ISA unless otherwise indicated.

Figure 6 shows that increasing the load factor applied to the body z-axis in the hover sizing condition results in a higher peak power availability from the electric motors. As expected, this additional power comes at the expense of an increase in the weight of the aircraft and an increase in the mass moments of inertia, also shown in in Figure 6.

Continuous Torque Limits at Hover

Under nominal hover conditions, it is required that the motors operate in the continuous operating range as depicted in Figure 4. This can be assessed by comparing the hover trims computed for design variants against the anticipated motor speed and torque limits, as shown in Figure 7.

The appearance of two distinct trim torque and speed values for each variant is due to the small difference in rotor speed between the fore and aft rotors required in a hover, with the aft rotors having the slightly higher rotor speed and torque requirements. Notably, Figure 7 illustrates a problem with the baseline 1.00 g design variant. The operating torque required to hover exceeds the continuous operation rated torque as indicated by the blue dashed line. Thus, this design would not be acceptable without modification, since nominal hover operations would require excessive torque output from the motors, resulting in impractically high motor temperatures (see Ref. 17 and Ref. 29). There are several approaches to resolving this problem, including some that involve changes to the motor specifications and modeling used in the NDARC sizing task. Here however, the design variants generated based on increased load factor are analyzed to determine which of the designs can trim to a hover with a motor rpm and motor torque within the continuous operating torque range, which as shown was satisfied by the 1.35 g design variant. Based on this observation, the design variants below 1.35 g load factor could be eliminated from further consideration. Nevertheless, to better illustrate performance among design variants, designs for less than the 1.35 g load factor will still be included in some subsequent analysis results.

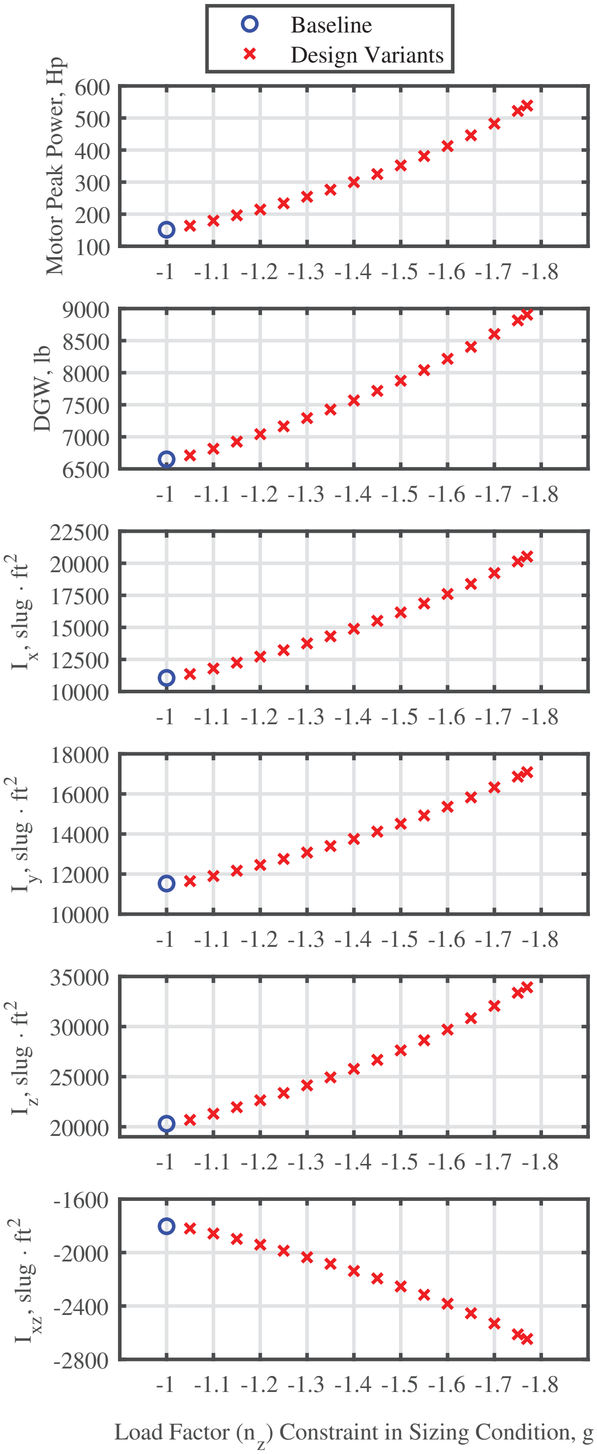

Figure 6: Motor power, design gross weight, and mass moments of inertia for all design variants as a function of the load factor constraint specified in the sizing task.

Hover Feasibility Following Motor Failure

Another important consideration is the feasibility of continued flight following the complete failure of a motor. Some UAM and AAM designs are expected to rely on motor redundancy for additional passenger safety in the event of failures. Because of aircraft symmetry, and for brevity of this discussion, only individual motor failures on motors 1 through 4 will be considered, but the analysis methods shown here should apply to any other combination of motor failures of interest. Flight following the failure of a motor will be modeled with the motor completely stopped and producing no lift; partial

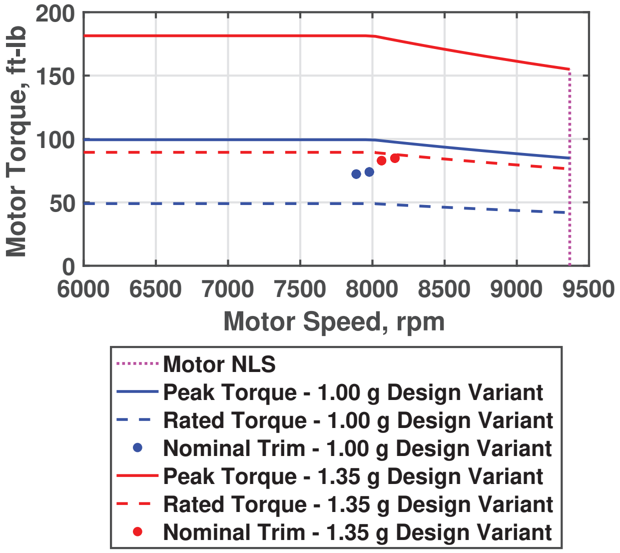

Figure 7: Motor speed and torque limits for baseline and 1.35 g design variant variants.

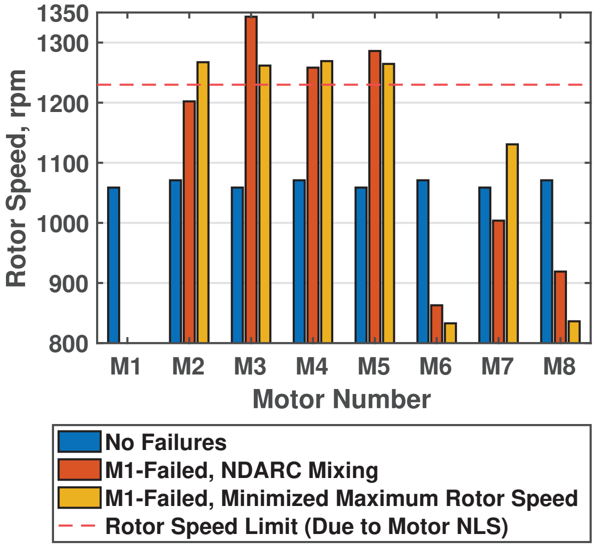

Figure 8: Comparison of hover condition trims under nominal and motor 1 failures, 1.35 g design variant, no gear ratio adjustment.

failures or stuck throttle failures were not considered. Each design variant was trimmed using MANITO to a hover condition with motors 1 through 4 individually failed. In the case of trimming with a motor failure, it should be noted that the default control mixing for this lift+cruise aircraft design as defined in NDARC (see Eq. 1) constrains the trim solution to needlessly high speeds on some motors. This occurs because the remaining seven motor speeds are being selected through only four inputs, which limits the available trim solution space to a subset of what the vehicle could achieve without mixing. This reduces the flexibility of the aircraft to respond to the failure, and in this case results in higher individual motors speeds than are strictly necessary, possibly causing a feasible failure scenario to appear infeasible.

As a demonstration of this, MANITO is used to trim the aircraft to a hover without any control mixing enforced and an objective function that penalizes maximum rotor speed. Figure 8 shows the rotor speeds found by trimming the 1.35 g design variant under nominal conditions with no motor failure, a failure of motor 1 with NDARC mixing enforced, and a failure of motor 1 with MANITO instructed to minimize the maximum motor speed. Figure 8 demonstrates that the optimization appears to succeed. Nevertheless, for this design a failure of motor 1 still results in motor speeds that slightly exceed the predicted motor NLS using the baseline design gear ratio.

Similar results are obtained for each of the individual motor failure scenarios, as shown in Figure 9. Here, the 1.35 g design variant is trimmed at a hover using MANITO to minimize the maximum motor speed for each motor failure case. Minor variations in maximum rotor speed occur due to the specific motor that is failed, but in each case the maximum rotor speeds exceed the rated NLS of the motors for the baseline gear ratio. This indicates a method of increasing the achievable rotor speed is necessary to produce an acceptable operating condition given the motor's limitations.

A more detailed look at this problem, and a potential solution, are illustrated in Figure 10 using a failure in motor 3 on the 1.50 g design variant as an example. Figure 10 shows the motor speed and motor torque required by all of the active motors, and includes both a nominal hover and motor 3 failed hover condition. For the baseline gear ratio factor of 1 (i.e., the original design in NDARC), a motor 3 failure results in several motors operating beyond the motor NLS rpm limit. Holding the rotor operating speed constant as required for the trim condition, the corresponding motor speed and torque can be modified by adjusting the gear ratio factor.

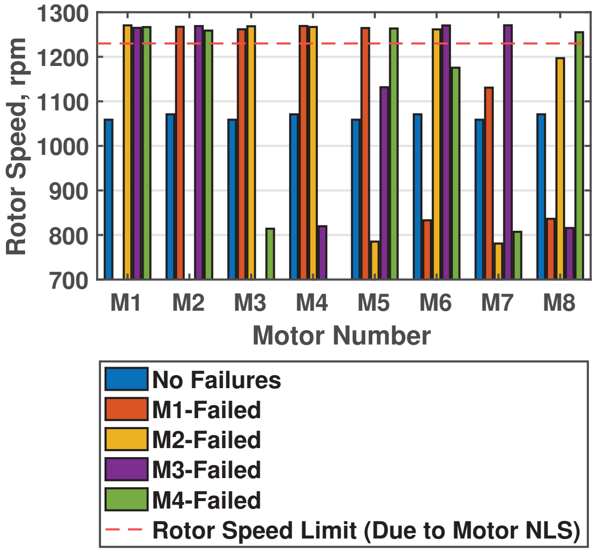

Figure 9: Nominal hover and motor failure cases for 1.35 g design variant. No gear ratio adjustment.

The nominal gear ratio (G_{r0}) of the baseline L+C NDARC design is 7.62, and in general the torque and speed relationships between the motors and rotors are $\omega_{motor} = G_{r0}\omega_{rotor}$ and $\tau_{motor} = \tau_{rotor}/G_{r0}$. By introducing a gear ratio adjustment factor by replacing G_{r0} with $G_{r0}G_{rf}$, and by maintaining the rotor speed and torque as required by the trim condition, the new motor speed and torque corresponding to the adjusted gear ratio can be computed. Note that this assumes negligible change in transmission losses by the introduction of this gear ratio adjustment factor. Figure 10 illustrates sweeping this adjustment factor from 1.0 to 0.5. As the gear ratio adjustment factor is reduced, the motor torque requirement increases while the motor speed requirement decreases, moving the trim conditions shown in Figure 10 upwards and towards the left side of the plot. For an adjustment factor of 0.85, both motor torque and motor speed required for a motor 3 failure fall well within the maximum motor torque and speed limits, indicating that continued flight following this failure may be feasible.

The gear ratio adjustment factor could be more precisely optimized given an appropriate selection criteria such as motor efficiency, but for the remainder of this analysis a value of $G_{rf} = 0.85$ will be used for demonstration purposes. Note that despite this adjustment, with motor 3 failed this design would be operating some motors in the intermittent load operating range, where problems associated with overheating and potential mechanical damage are expected. Thus, according to this motor model, operations following a motor failure for this variant would need to be of limited duration. Also of concern is that by adjusting the gear ratio to accommodate motor failures, the motor speed and torque required for nominal hover also shifts. For a 0.85 gear ratio factor, several of the lower motor power variants exceed their continuous operating torque limit, and analysis shows that the 1.45 g design variant becomes the minimum necessary to obtain a nominal hover-trim motor torque in the continuous operating range of the motors.

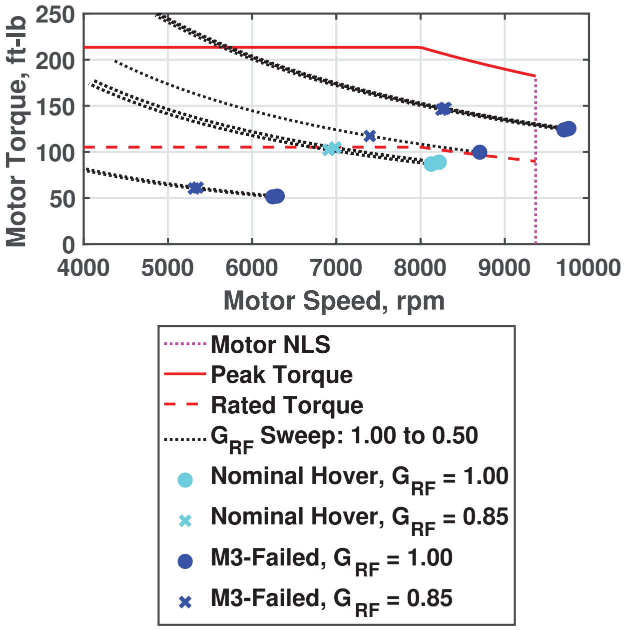

Figure 10: Gear ratio adjustment factor selection based on motor 3 failure for 1.50 g variant.

The primary purpose of this example is to illustrate that design trade-offs are complicated by the requirement to accommodate motor failures while also designing for efficient nominal performance, vehicle weight, and cost. Ideally, these relationships could be incorporated directly into the sizing task to minimize the time required to analyze design variants under each scenario of interest. However, several of the capabilities required to do this reliably are not included in NDARC version 1.18a, and were here supported using the external tools developed for trim optimization, mass MOI estimation, and electric motor performance modeling described in this paper. For the purposes of this study, the analysis will proceed with the design variants as previously described, with an adjustment of a gear ratio factor of 0.85, since this allows further study of the handling qualities and performance characteristics of the aircraft following a motor failure while still accounting for the anticipated motor speed and torque limits.

Estimating Feasible Maneuverability Via Convex Optimization

In order to quantify the limits of vehicle maneuvering performance, convex optimization was utilized to compute the maximum feasible amplitude of periodic angular velocity in selected directions at specified frequencies. Both nominal and failure conditions were analyzed using identical methods in order to capture the impact of the failures on the feasible maneuverability of the aircraft. Each linear model used is based on a trim associated with the operating condition (i.e., nominal hover, motor 1 failed hover, etc.), and on the specific design variant under consideration (i.e., 1.25 g, 1.50 g, etc.). It should be noted that the motion of the vehicle computed by this approach, especially for low frequencies where the feasible motion is very large, will often exceed the validity range of the linear dynamics approximation. For these cases, the results should be interpreted as quantitative metrics offering some measure of relative maneuvering capability rather than a reliably precise estimate of what the real aircraft would be capable of.

The convex optimization problems took about 0.1 seconds to solve on average. These were all computed using a single core on an Apple M3 Pro processor, with the combined 31,450 unique periodic trajectories taking about 52 minutes to solve, or about 3 minutes per design variant. Parallelization and efficiency improvements are undoubtedly possible and could be used to substantially reduce this time, such that computational cost does not appear to be a major limitation of this analysis technique.

Maximum Amplitude Periodic Motion Figure 11 illustrates a time history of angular velocity for a typical convex optimization result, with the corresponding torque inputs shown in Figure 12. Here, the desired motion was rotation about the x-axis (i.e., roll) in the body coordinate system, such that the control coordinate system and body coordinate system were identical. The maximum achievable sinusoidal amplitude was computed as 3.03 rad/s for this design variant, operating condition, angular frequency, and direction. It is worth emphasizing that the very large roll rate computed is not intended to represent realistic flight conditions; rather, it should be interpreted simply as a metric that measures properties of the vehicle design, accounting for influences like control effector saturation limits, aircraft mass moment of inertia, and other dynamics captured by the model. The angular frequency of the required velocity variation is 1 rad/s which produces a period of 2π seconds. The bounds on both on-axis and off-axis motion are shown, illustrating that the computed solution does not violate them. As could be expected for this optimal control problem, the inputs to the system (here, motor torque) change abruptly between the bounds, as shown in Figure 12. Since the desired motion is in the roll axis, the saturated inputs are seen to alternate between left (M1 through M4) and right (M5 through M8) wing motors, generating an aggressive peak roll rate.

Motor speed follows the expected pattern as well given these inputs, closely approaching saturation against the motor NLS limits as shown by Figure 13. To better visualize how the motor torque and motor speed limits influence the solution, it is helpful to plot the optimal trajectory in terms of motor speed and torque, as show in Figure 14. Here, it is observed that the upper and lower torque limits are frequently reached, including the reduced torque limit area beyond 8000 rpm. The motor NLS limit is also closely approached by the solution trajectory, but does not remain saturated against this limit for any substantial period of time. Thus, for this operating condition, direction of motion, sinusoidal frequency, and design variant, it could be concluded that the roll agility appears to be primarily limited by torque margin availability.

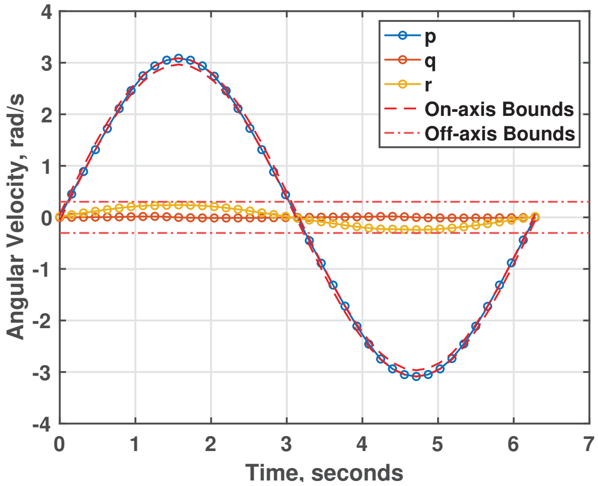

Figure 11: Angular velocity for maximum feasible amplitude 1 rad/s sinusoidal tracking for roll rate, nominal hover operating condition, 1.45 g design variant.

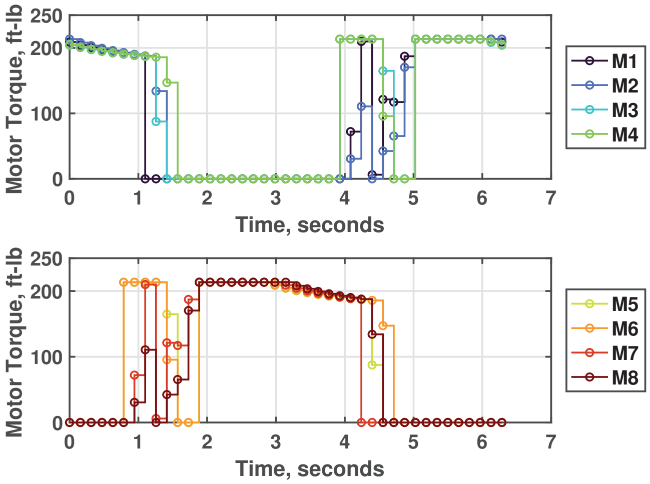

Figure 12: Motor torque for maximum feasible amplitude 1 rad/s sinusoidal tracking for roll rate, nominal hover operating condition, 1.45 g design variant.

As an example of an operating condition for which motor speed limits plays a more significant role, consider also the 1.75 g design variant under the same analysis conditions, looking first at motor torque as shown in Figure 15. Comparing Figures 12 and 15, it is apparent that there are some differences in the torque inputs required for the maximum amplitude solution. These differences are due in part to the increased impact of the motor speed limit on the trajectory, as illustrated in Figure 16.

For this variant and operating condition, both the motor speed and motor torque limits act as active constraints on the achievable sinusoidal amplitude, which is illustrated by Figure 17. The maximum achievable amplitude for this design variant and operating conditions was found to be 3.36 rad/s, which is only slightly larger than was obtained for the 1.45 g design

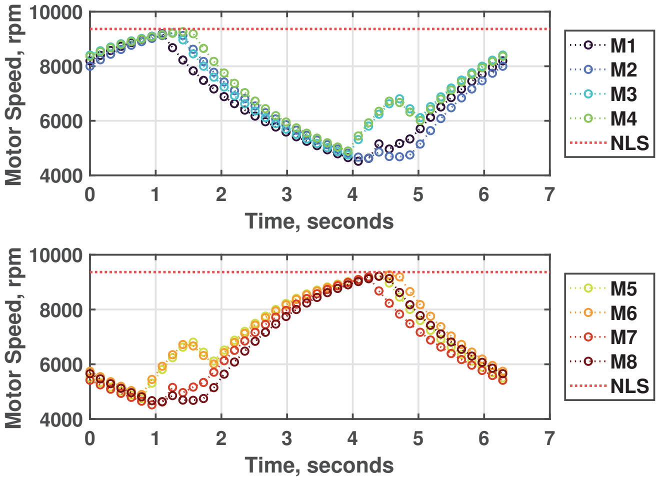

Figure 13: Motor speed for maximum feasible amplitude 1 rad/s sinusoidal tracking for roll rate, nominal hover operating condition, 1.45 g design variant.

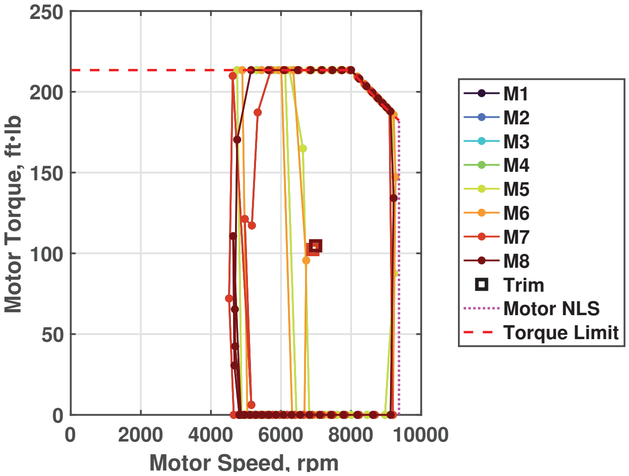

Figure 14: Motor torque and speed maximum feasible amplitude 1 rad/s sinusoidal tracking for roll rate, nominal hover operating condition, 1.45 g design variant.

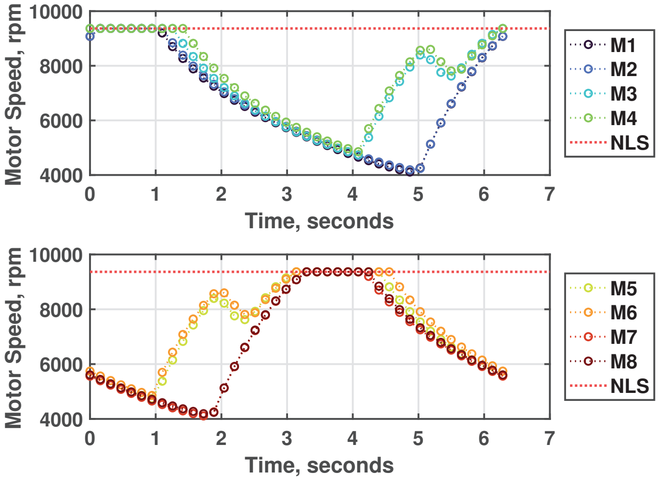

Figure 16: Motor speed for maximum feasible amplitude 1 rad/s sinusoidal tracking for roll rate, nominal hover operating condition, 1.75 g design variant.

variant.

In order to analyze the directional sensitivity and frequency dependence of the maximum feasible angular acceleration for variants and failure scenarios, comparison plots can be used. Note that while the specified trajectory for computing the optimal trajectory was in terms of a sinusoidal angular velocity requirement, the corresponding angular acceleration can be determined as $a\omega\cos(\omega t)$, such that the sinusoidal acceleration magnitude can be estimated as $a\omega$, allowing for some error due to ε_{track} which here is assumed to be negligible.

Figure 18 shows the maximum amplitude of periodic angular acceleration in body roll ($\dot{p}$), pitch ($\dot{q}$), and yaw ($\dot{r}$) directions, as well as the combined volume of achievable angular acceleration amplitude across the spherically sampled directions shown in Figure 5. For $\dot{p}$ and $\dot{q}$, there is a substantial reduction in achievable magnitude with frequency. However, maximum $\dot{r}$ amplitude is considerably less sensitive to frequency. This can be explained based on the fundamental physics of the vehicle. Roll and pitch moments are generated by changing rotor speed to generate thrust, but desired changes in rotor speed cannot occur instantaneously as a response to rotor shaft torque inputs. Conversely, the dynamics model used here assumes that the torque applied to the rotor shaft is able to be commanded directly and instantaneously to any desired value within the torque limits. Since yaw moment is primarily generated by rotor shaft torque for this aircraft in a hover, it is unsurprising that $\dot{r}$ displays little frequency dependence. The slight reduction in attainable $\dot{r}$ amplitude as frequency increases can be attributed to the cant angle of the inboard rotors, which creates a rotor speed contribution to yaw moment. Each of the angular acceleration plots in Figure 18 illustrate that the variants sized to have additional available

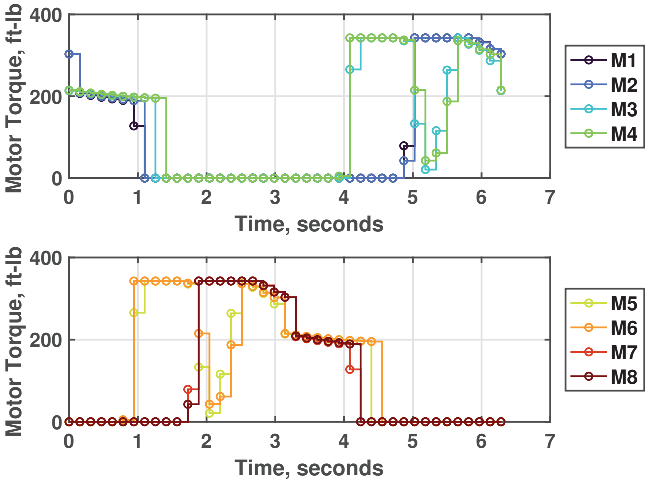

Figure 15: Motor torque for maximum feasible amplitude 1 rad/s sinusoidal tracking for roll rate, nominal hover operating condition, 1.75 g design variant.

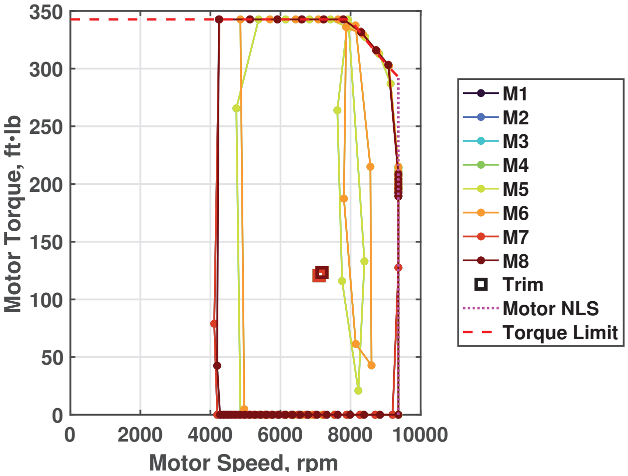

Figure 17: Motor torque for maximum feasible amplitude 1 rad/s sinusoidal tracking for roll rate, nominal hover operating condition, 1.75 g design variant.

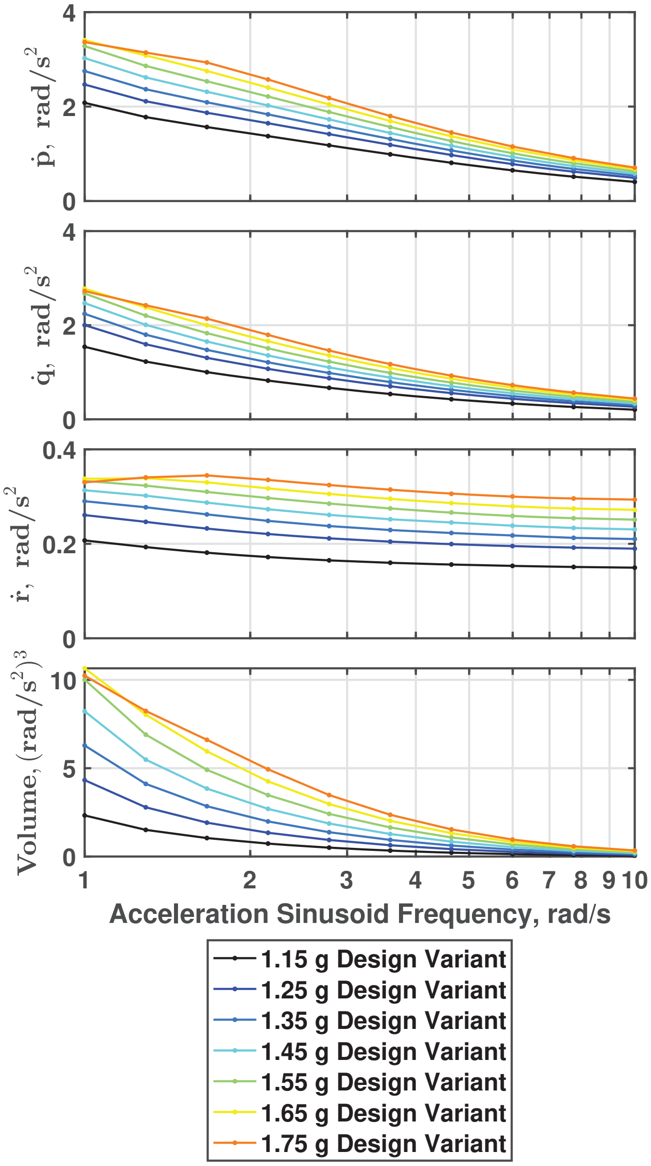

Figure 18: Nominal hover maximum angular acceleration for selected variants, no failures.

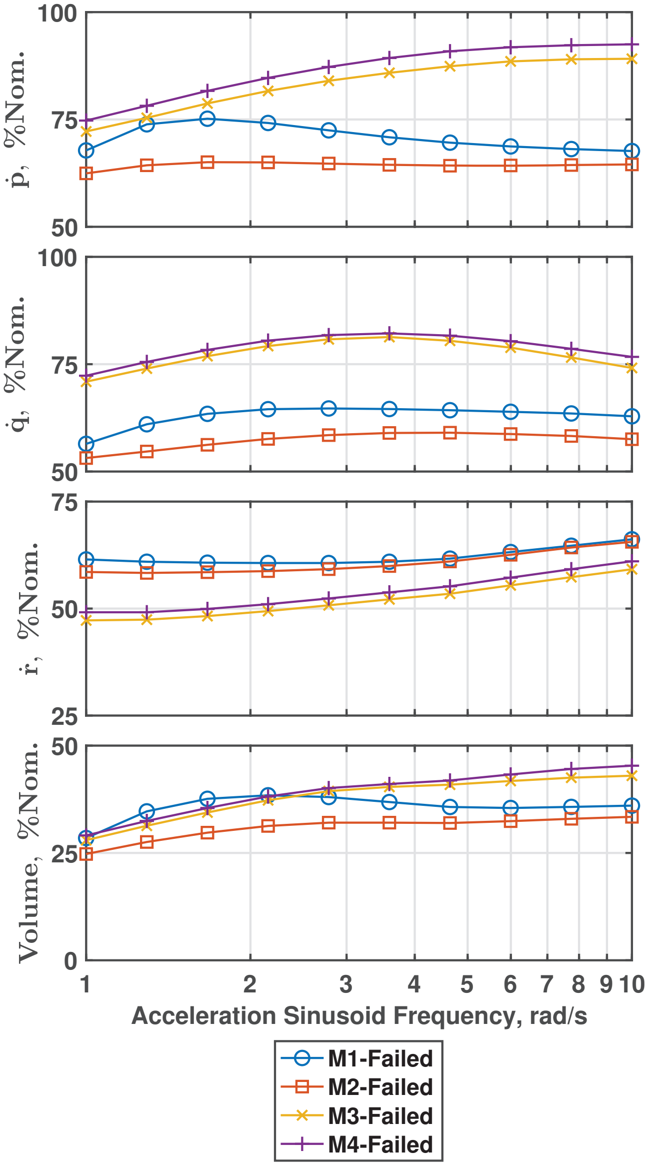

Figure 19: Maximum angular acceleration for various motor failure scenarios, normalized by nominal condition results, 1.45 g design variant.

motor power and torque typically produce higher feasible acceleration magnitudes. However, at low frequencies there is a diminishing return observed for some of the highest power variants. This is primarily due to the motor NLS being held constant during the sizing of all design variants, resulting in the motor NLS playing a more significant role in constraining the performance of the heavier design variants, especially at lower frequencies where the motor-speed variation is often large.

Motor failure scenarios can be analyzed similarly, with results normalized by the no-failure maximum angular acceleration amplitude as shown in Figure 19, from which several conclusions of interest can be drawn. First, note that for both $\dot{p}$ and $\dot{q}$, a failure of motor 2 is predicted to have the highest impact on performance, which is also reflected in the total volume plot at the bottom of Figure 19. Also, outboard motor failures (motors 1 and 2) have a larger impact on $\dot{p}$ and $\dot{q}$ capability, while motor 3 and 4 failures have a larger impact on $\dot{r}$ due to the cant angle of these motors. The percentage reduction in maneuverability varies with frequency, but not dramatically for this example.

However, note that following a motor 3 or motor 4 failure, achievable $\dot{p}$ amplitude is roughly 90% of nominal at high frequencies for this variant, indicating that high-frequency roll acceleration might not be dramatically affected about this trim condition. Surprisingly, for the 1.75 g variant with motor 3 or 4 failed, the achievable $\dot{p}$ increases slightly beyond 100% of the nominal operating condition at the highest angular frequency of 10 rad/s, suggesting higher attitude responsiveness might be possible at these trims following a motor failure. This is explained by the trim condition for

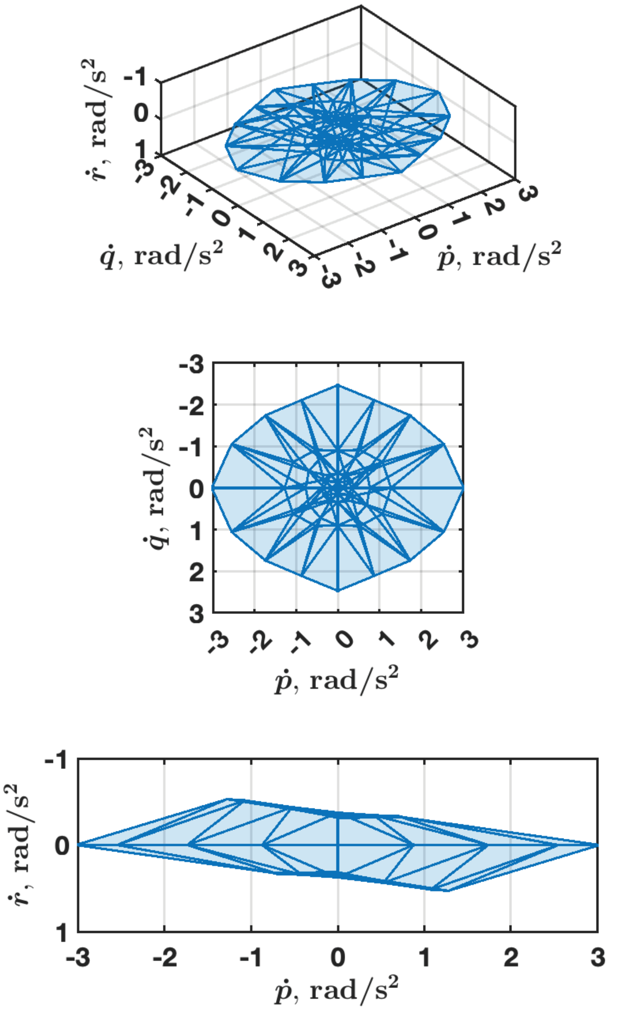

Figure 20: Maximum sinusoidal angular acceleration volume, 1 rad/s, nominal hover operating condition, 1.45 g design variant.

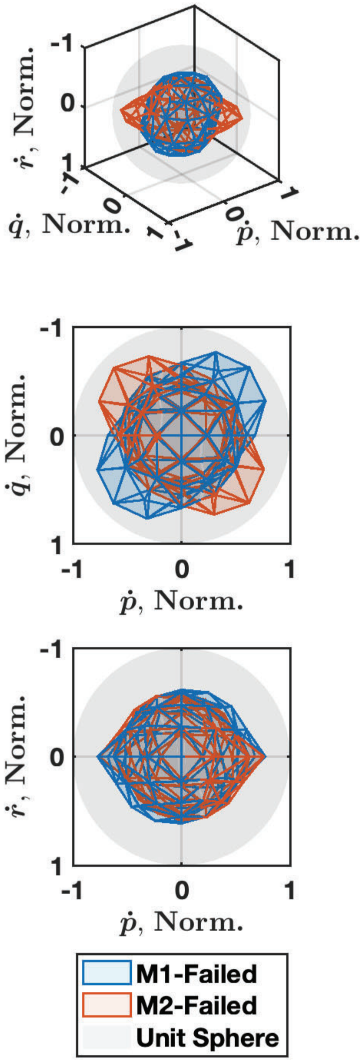

Figure 21: Maximum angular acceleration for motor 1 and motor 2 failure cases normalized by no-failure case, 1 rad/s sinusoidal angular velocity, hover operating condition, 1.45 g design variant.

these inboard motor failures (see Figure 9) requiring significantly higher rotor speeds from the outboard motors, which increases the linear-model's partial derivative gain between rpm changes and thrust (and thus roll moment) due to the underlying quadratic increase in thrust as a function of rotor speed. This suggests there may be significant value in intentionally trimming to maximally maneuverable trims, which could be done to mitigate maneuverability loss following a failure, or even to increase nominal maneuverability by optimizing the distribution of rotor lift in a way that increases responsiveness. This approach to selecting among feasible operating conditions might be especially important during certain phases of flight where maximum maneuverability is critical.

The three dimensional volume formed by the maximum achievable amplitudes in each of the sampled directions is also of interest, and is shown in Figure 20. First, it is notable that there is considerably more angular acceleration possible in pitch ($\dot{q}$) and roll ($\dot{p}$) than in yaw ($\dot{r}$) at this frequency. The aircraft is slightly more capable of $\dot{p}$ than $\dot{q}$, but the difference is small. Looking at similar depictions as frequency increases reveals that the $\dot{p}$ and $\dot{q}$ limits decrease more that $\dot{r}$, which is also indicated by Figure 18. Thus, at high frequencies, $\dot{p}$, $\dot{q}$, and $\dot{r}$ capabilities become more similar to one another.

To analyze the directional impact of motor failure or other off-nominal scenarios, a visualization such as Figure 21 is useful. Here, the maximum feasible amplitude in each direction for a failure scenario is normalized by the amplitude obtained at the nominal operating condition. These normalized amplitudes can be plotted in the corresponding directions, providing a visual representation of the relative impact of the off-nominal scenario in each direction. For each point on the surface, a distance from the origin of less than 1 represents a reduction of achievable maximum acceleration amplitude in that direction. For the motor 1 failure scenario, the middle plot of Figure 21 shows substantially reduced maneuverability across the

$p = q$ axis, which corresponds to in-phase positive roll and pitch motion. Conversely, motion about the $p = -q$ axis is far less attenuated by a motor 1 failure. Interestingly, for a motor 2 failure, the opposite relationship is observed. For these simple examples, the asymmetry can be understood intuitively by considering the locations of motor 1 and 2 and the corresponding moments that they generate via thrust. However, for more complex aircraft or operating conditions, the asymmetric performance implications of some failures might be less obvious, making visualization techniques such as Figure 21 helpful in exploring the maneuvering impact of these conditions.

Feasible Performance Criterion Parameters for Moderate-Amplitude Attitude Changes An estimation of an upper bound on feasible handling qualities performance criterion parameters for moderate-amplitude attitude changes was completed for each variant in nominal and motor failure conditions using the Attitude Quickness criterion boundaries from ADS-33E-PRF and MIL-DTL-32742. It is emphasized that no feedback controller is being designed or implemented here. Instead, the trajectory generated is only a function of the convex optimization constraints and quadratic cost function as given in Eq. 23. Thus, these results should be interpreted as an estimated upper limit on the feasible performance criterion parameters of each vehicle design variant given the modeled aircraft dynamics and motor torque and speed constraints, rather than a prediction of how a specific control strategy will perform.

A time history of roll angle response is shown in Figure 22 for a selection of variants under nominal and motor 2 failure conditions, and target roll angles ranging from 5° to 60°. The peak roll rate p_{pk}, peak roll angle attitude change $\Delta\phi_{pk}$, and minimum roll angle attitude change $\Delta\phi_{min}$ as defined in ADS-33E-PRF (Ref. 32) were identified from these time histories, and used to evaluate the performance of the Attitude Quickness criterion as shown in Figure 23. The rating levels (for example, “Level 1”) indicated in Figures 23 and 24 refer to the predicted Cooper-Harper Handling Qualities Ratings, with Level 1 indicating satisfactory performance without design modification, Level 2 indicating deficiencies warranting improvement, and Level 3 indicating deficiencies requiring improvement (Ref. 32). It is apparent that the increased motor power variants produce increased performance, but perhaps with somewhat diminishing improvement as power increases. The design variants considered under nominal (no failure) operating conditions are capable of achieving peak roll rate to roll attitude change ratios well within the predicted Level 1 handling qualities region. Performance degradation is observed in the motor 2 failure scenarios, as expected and suggested by the earlier results shown in Figure 19, with the performance of the 1.25 g variant entering the Level 2 region. However, the 1.45 g and 1.65 g variants produce feasible trajectories in the Level 1 region for the motor 2 failure cases, suggesting that with appropriate control system design it may be possible to avoid a problematic handling qualities degradation for this axis and response type.

Similar analysis was completed to evaluate moderate-amplitude heading attitude changes, as shown in Figure 24. Under nominal operating conditions, the results indicate that it is feasible for all three design variants shown to meet the requirement for prediction of Level 1 handling qualities based on this criterion. However, a failure of motor 3 significantly lowers achievable performance in the yaw axis, with performance degrading to the boundary between Level 1 and Level 2 regions for heading changes above 20°. This suggests that control design targeting performance in the Level 1 region following a motor 3 failure may prove very challenging regardless of how much marginal torque is added to the lifting motors using the sizing methods employed in this paper.

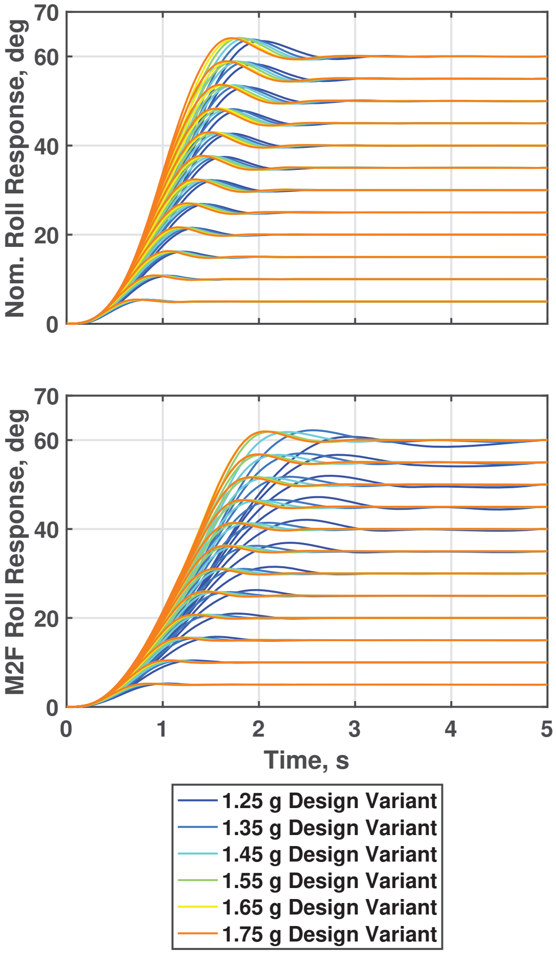

Figure 22: Roll response convex optimization time history, selected design variants at nominal (Nom.) and motor 2 failure (M2F) hover conditions.

Overall, the results from this section demonstrate the utility of the convex optimization analysis methods. The techniques appears well-suited to revealing deficiencies and quantifying differences between design variants that might otherwise be hard to capture. They might also be useful for forming metrics to optimize trim conditions for aircraft with redundant control effectors.

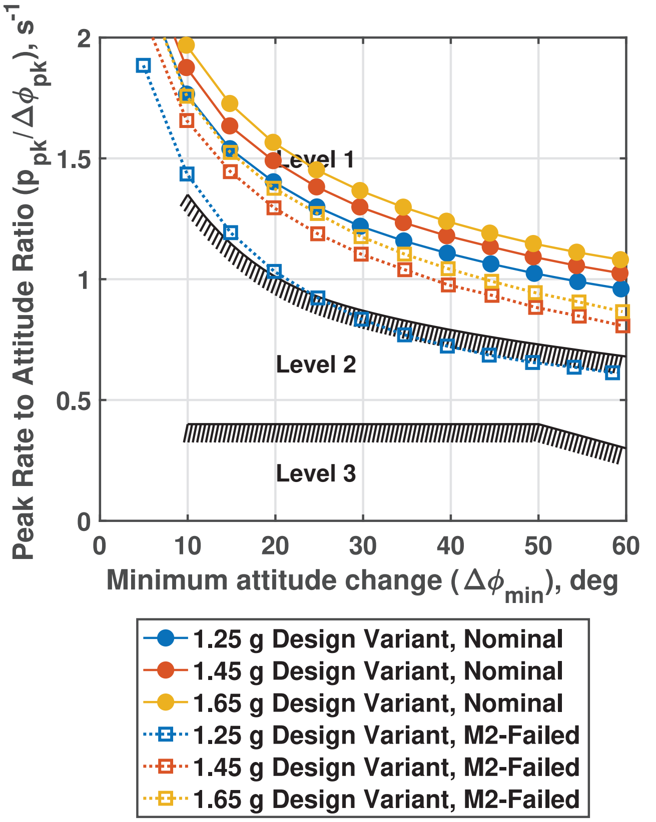

Figure 23: Roll Attitude Quickness convex optimization results, selected design variants at nominal and motor 2 failure hover conditions.

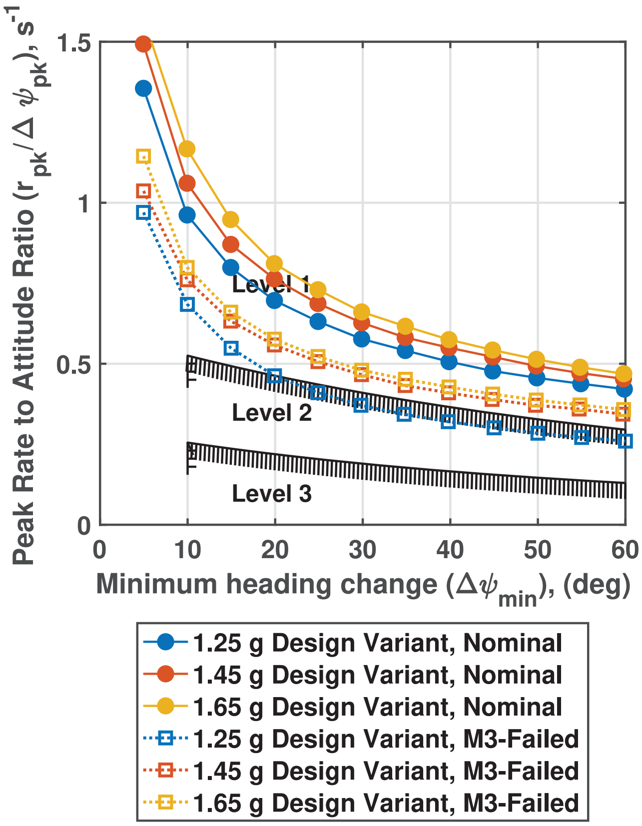

Figure 24: Yaw Attitude Quickness convex optimization results, selected variants under nominal and motor 3 failure conditions.

Control System Performance

Following the feasibility analysis using the convex optimization methods, a feedback control system for hover conditions was developed for a subset of the design variants. The purpose of the control system analysis was to evaluate the motor torque and speed responses relative to their respective limits for each design variant. Additionally, it allows for comparisons of the closed-loop system performance to the feasibility analysis results.

The control system parameters were tuned to meet a set of stability, handling-qualities, and performance specifications. Phase and gain margin requirements were based on SAE AS 94900 (Ref. 34) and predicted handling qualities specifications were selected from MIL-DTL-32742 (Ref. 33). A top-level block diagram of the control system is shown in Figure 25 and the response-types for the roll, pitch, yaw, and heave axes are listed in Table 3.

Table 3: Control system response-types.

Axis	Response-Type
Roll	Attitude Command/Attitude Hold (ACAH)
Pitch	Attitude Command/Attitude Hold (ACAH)
Yaw	Rate Command/Direction Hold (RCDH)
Heave	Rate Command/Height Hold (RCHH)

The pilot input vector δ has four channels for lateral δ_{lat}, longitudinal δ_{lon}, pedal δ_{ped}, and vertical rate δ_{V_z} inputs. Parameters in the command model were selected to target desired performance for small and moderate-amplitude response requirements, while the feedback gains were tuned to meet disturbance rejection and stability margin requirements. A robust servo-mechanism linear quadratic regulator (RSLQR) structure was used to provide reference tracking with feedback stabilization (Ref. 40). The RSLQR approach allows for augmentation of the linear dynamics state-space model to include error signals for command following with zero steady-state error. States for the error signals were defined to apply integral action to the aircraft attitude angles (ϕ, θ, and ψ) and vertical velocity. The feedback gain matrix was computed by applying the LQR algorithm to the augmented state-space representation with specified cost function parameters Q and R. An unconstrained nonlinear programming solver was used to determine the weights in the Q and R matrices that met requirements for user-defined values of disturbance rejection bandwidth (DRB) and disturbance rejection peak (DRP), as defined in MIL-DTL-32742. Table 4 lists the targeted disturbance rejection performance for each axis, and performance criterion parameters for small-amplitude attitude change requirements (bandwidth ω_{bw} and phase delay τ_p). This approach ensured that the control system for each design variant had similar disturbance rejection and piloted re-

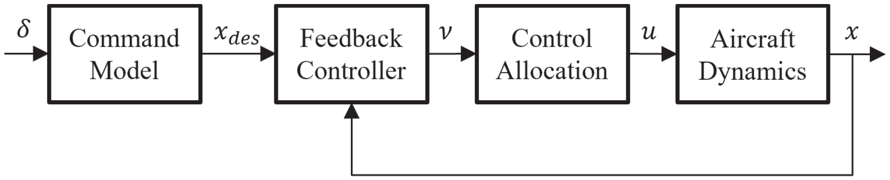

Figure 25: Control system diagram.

sponse characteristics, facilitating comparisons of variant performance. A vector of commanded body-axis moments and vertical acceleration ν was mapped to a control input vector u using a mixer matrix, which was computed using a weighted pseudo-inverse. The control system was designed for hover and low-speed conditions and excluded consideration of transition; therefore, the only control actuators that were included were the electric motors that drive the lifting rotors. The trailing edge control surfaces and pusher prop were not used. The control system was implemented for the nominal hover models (no failure) for the 1.25 g to 1.75 g design variants.

Table 4: Design points for control system development.

Specification	**Roll**	**Pitch**	**Yaw**	**Heave**
DRB (rad/s)	0.9	0.8	0.75	1
DRP	2.5	2	3	2.5
ω_{BW} (rad/s)	2.5	2.5	1	0.7
τ_p (s)	0.15	0.15	0.2	0.1

Figures 26, 27, 28, and 29 show linear simulation results for roll, pitch, yaw, and vertical rate step inputs for the 1.45 g design variant. The amplitude was 10 deg for roll and pitch, 10 deg/s for yaw rate, and 600 ft/min for vertical rate inputs. The on-axis responses, rotor speeds, and motor torques are shown on each plot. The motor torque responses indicate that the control mixer allocates the torque demands based on control effectiveness for each axis. Figure 26 show that the mixer allocates higher amplitude torque demands to the outboard motors, which is due to their larger moment arm relative to the center of mass in comparison to the inboard motors. In Figure 27, the control mixer achieves the desired body-axis pitching moment by splitting torque allocation between the front and rear motors. For yaw control, motor torques relate directly to body-axis yawing moment, therefore the mixer applies differential torque commands to the CCW and CW motors, as shown in Figure 28. Increasing the amplitude of these step inputs will lead to motor torque saturation, resulting in degraded responses, off-axis coupling, and potential instability.

The design variants sized for larger load factors tend to provide an increased torque margin. However, their increased weight and moment of inertia values lead to an increase in the power required to achieve similar piloted response and disturbance rejection characteristics. Figure 30 shows the minimum torque margin and increase in motor torque root mean square (RMS) for a subset of the design variants for the step responses with the same amplitude as Figures 26 through 29. The torque margin was computed by taking the difference between the maximum torque demand across all motors in the time history response and the motor's available peak torque, and then dividing by the peak torque. The actuator RMS is expressed as a percent increase relative to the 1.45 g design variant to provide a measure of relative increase in power consumption. These results help to quantify the trade-off between available actuator margin and power consumption requirements.

In order to allow comparisons with the convex optimization results for yaw Attitude Quickness, yaw pulse inputs were applied through the pilot input to selected design variants with the motor torque and motor NLS limits enforced. The pulses were 1 second in width, with a range of amplitudes applied. The Attitude Quickness performance is shown in Figure 31 for amplitudes in which the response remained stable. The "Estimated Bound" values that are plotted reflect the convex optimization results and are identical to the "Nominal" data shown in Figure 24. The responses at $\Delta\psi_{min} = 10°$ are effectively identical for all design variants under feedback control because each was tuned to produce the same piloted response characteristics. However, the effects of saturation become apparent as the amplitude of the heading change increases. The 1.25 g variant performance degrades rapidly as amplitude increases beyond 10°, with heading changes above about 25° causing oscillatory behavior and a reduction in both $r_{pk}/\Delta\psi_{pk}$ and $\Delta\psi_{min}$. Similar results occur for the 1.45 g design variant, though at a higher heading change amplitude of about 30°. For the amplitudes shown, the 1.45 g and 1.65 g design variants maintain responses in the Level 1 region and are bounded above by the convex optimization results as expected. The smaller design variants experience performance degradation as the change in heading increases in magnitude, indicating that the control system implemented is not able to effectively deal with the control effector saturation.

The preliminary results from the control system implementation and analysis provide insights into the trade-offs between power consumption requirements and increased torque margin. Additionally, comparison of the Yaw Attitude Quickness criteria results support the validity of the feasible limits predicted using convex optimization. Evaluation of the step responses of the 1.45 g variant show that the motor torque demands from the control system are within 20% of the motor's rated peak torque for the step command amplitude. This suggests that larger motors or control system design changes would likely be required to avoid hitting saturation limits during large-amplitude attitude changes.

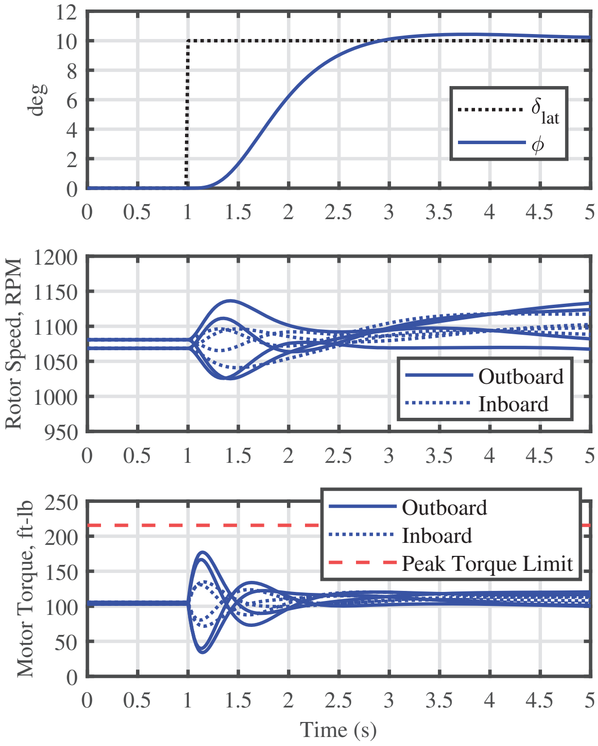

Figure 26: Roll step response, 1.45 g design variant, nominal hover.

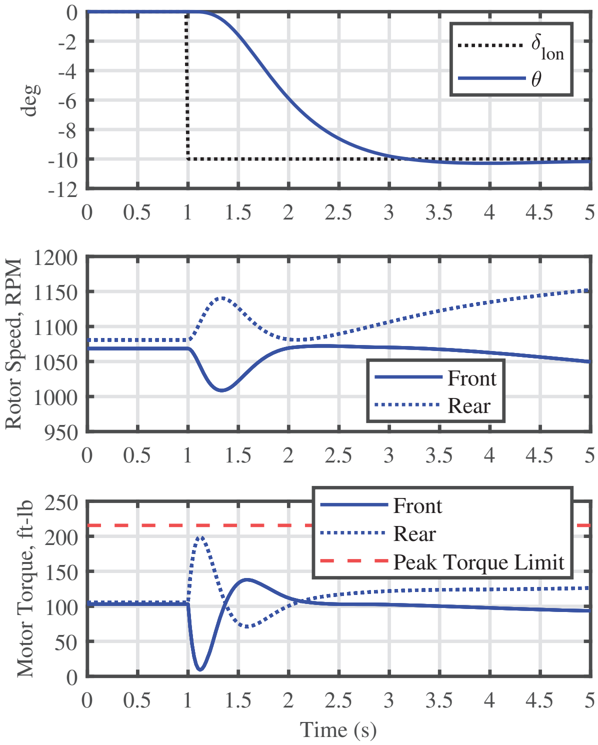

Figure 27: Pitch step response, 1.45 g design variant, nominal hover.

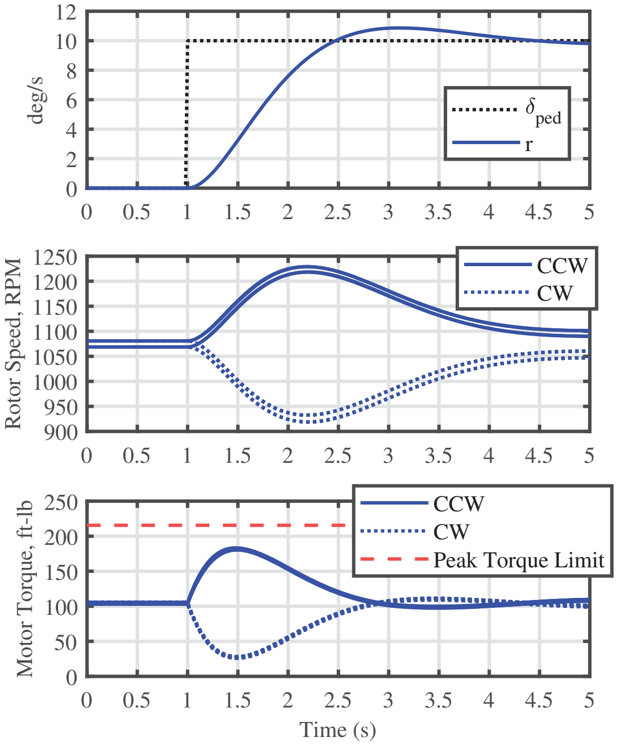

Figure 28: Yaw rate step response, 1.45 g design variant, nominal hover.

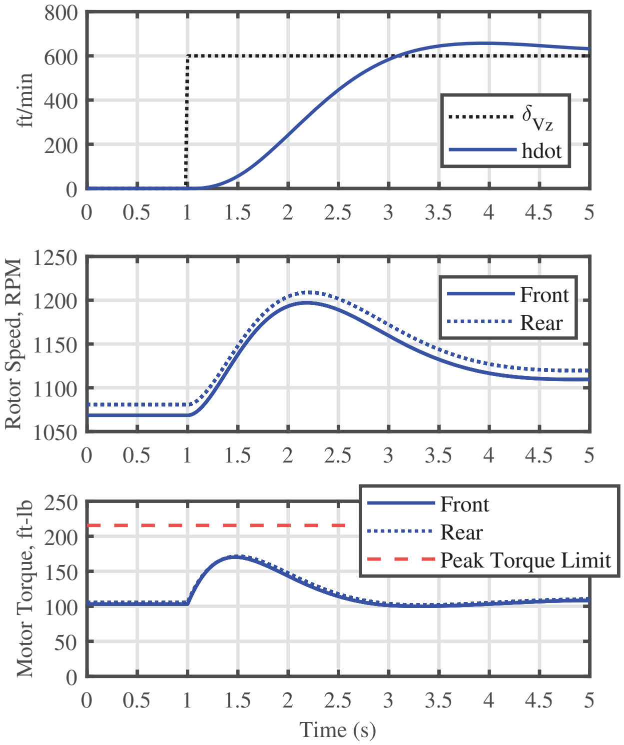

Figure 29: Vertical rate step response, 1.45 g design variant, nominal hover.

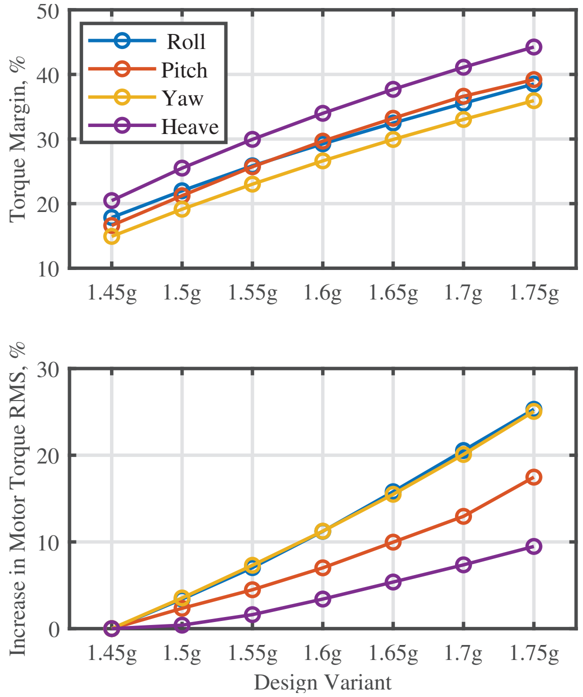

Figure 30: Torque margins and increase in actuator RMS based on piloted step inputs for each axis.

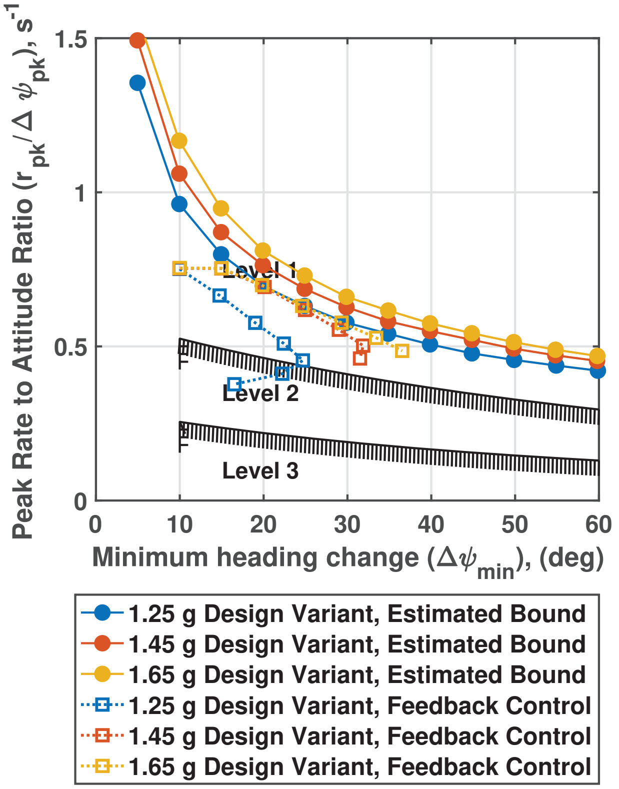

Figure 31: Yaw Attitude Quickness comparing convex optimization upper bound estimate with feedback control system implemented for selected variants under nominal no-failure hover conditions.

CONCLUSIONS

The following remarks summarize observations and results from this paper.

1. Redundantly actuated aircraft often have non-unique trim solutions for some operating conditions. Computing appropriate trims within the set of available solutions can be an important aspect of analyzing a vehicle's predicted performance, establishing the feasibility of sustained flight following a failure scenario, and producing linear models. A trim optimization tool that interfaces with NDARC to externally compute trim solutions was developed and demonstrated. The tool was used in failed motor scenarios to compute hover trims that minimized the maximum rotor speed, helping to produce larger torque and speed margins for the remaining motors under these conditions than could be obtained using the baseline control mixing for the lift+cruise.
2. An assumption of constant radius of gyration values may not be adequately accurate for some sizing studies. Estimating the mass MOI matrix using a component-by-component build-up approach may produce more reliable results and better capture fundamental trade-offs during sizing studies where attitude control is important and mass is being distributed differently between design variants. A tool was developed and demonstrated to rapidly generate MOI estimates based on NDARC sizing output, and was found to offer improved reliability.
3. Motor performance limitations such as torque and speed limits directly contribute to the maneuvering capabilities of fixed-pitch variable-speed rotorcraft designs. Establishing realistic predictions of motor performance can improve handling qualities predictions, especially in off-nominal or failure scenarios in which the design might be stressed in ways not easily accounted for in the basic sizing mission. Investment in reliable modeling of these components appears worthwhile and can increase confidence in a trade-study involving motor sizing.
4. Convex optimization in combination with appropriately formulated problems can offer an attractive complement to other approaches for analyzing predicted handling qualities early in the design process. In some applications, this might enable faster and more reliable analysis of a design's feasible performance capabilities than would otherwise be possible. These methods might be used to establish upper limits on achievable vehicle performance, select favorable trim conditions, quantify trade-offs between vehicle design variants, and may be useful in identifying and solving design deficiencies. Importantly, the methods presented in this paper do not require control system design, control allocation, or tuning to be utilized. The maximum angular velocity sinusoidal tracking convex optimization problems were formulated to support analysis of motion in arbitrary directions and at different frequencies, with the results serving as a useful metric for comparing the relative perfor-

mance of design variants and operating conditions. The moderate-amplitude attitude change responses generated using convex optimization also provide a useful estimate of the upper bound on the Attitude Quickness Criteria. This method may be particularly useful for establishing the feasibility of achieving predicted Level 1 handling qualities under various failure scenarios.

5. A preliminary assessment of a hover control system was presented with examples of piloted step responses for each axis. The results help quantify the trade-off between available actuator margin and power consumption requirements to achieve consistent disturbance rejection and piloted response characteristics. The Yaw Attitude Quickness criterion was also evaluated over a range of heading changes, with results supporting the validity of the convex optimization estimates for upper bounds on achievable performance.

Author contact: David Hartman, david.c.hartman@nasa.gov; George Altamirano, george.altamirano@nasa.gov; Peter Suh, peter.m.suh@nasa.gov.

ACKNOWLEDGMENTS

The authors thank Justin Matt and Thomas Ivanco of NASA Langley Research Center, and Jeremy Aires of NASA Ames Research Center, for their helpful reviews of this paper. This research was funded under the NASA Revolutionary Vertical Lift Technology (RVLT) project.

REFERENCES

1. Federal Aviation Administration, "Advanced Air Mobility (AAM) Implementation Plan: Near-Term Focus with an Eye on the Future of AAM, Version 1.0," Technical report, Federal Aviation Administration, July 2023.

2. Chakraborty, I., and Mishra, A., "Generalized Energy-Based Flight Vehicle Sizing and Performance Analysis Methodology," *Journal of Aircraft*, Vol. 58, (4), 2021, pp. 762–780. DOI: 10.2514/1.C036101.

3. Chakraborty, I., and Mishra, A., "Sizing and Analysis of a Lift-Plus-Cruise Aircraft with Electrified Propulsion," *Journal of Aircraft*, Vol. 60, (3), 2023, pp. 747–765. DOI: 10.2514/1.C037044.

4. Mishra, A., Comer, A., and Chakraborty, I., "AMS-Based Integration of Flight Dynamics and Control in a Vectored Thrust UAM Vehicle Design," Paper AIAA 2025-2349, AIAA SciTech 2025 Forum, Orlando, FL, Jan 6–10, 2025.

5. Chakraborty, I., and Mishra, A., "Sizing of Tilt-Wing Aircraft with All-Electric and Hybrid-Electric Propulsion," *Journal of Aircraft*, Vol. 60, (1), 2023, pp. 245–264. DOI: 10.2514/1.C036813.

6. Saetti, U., and Bugday, B., "Generic Tilt-Rotor Simulation Model with Coupled Flight Dynamics, State-Variable Aeromechanics, and Aeroacoustics," VFS International 79 th Annual Forum & Technology Display, West Palm Beach, FL, May 16–19, 2023.

7. Gladfelter, M., He, C., Saberi, H., Malpica, C., Johnson, W., and Silva, C., "Enhanced Flight Dynamics Models with Aerodynamic Interference for Real-Time Simulation of VTOL Concept Vehicles," Proceedings of the VFS International 79th Annual Forum & Technology Display, May 2023.

8. Alvarez, E., and Ning, A., "High-Fidelity Modeling of Multirotor Aerodynamic Interactions for Aircraft Design," *Journal of Aircraft*, Vol. 58, (10), 2020.

9. Research in Flight, "FlightStream®: Fast Aerodynamics with Fidelity," https://researchinflight.com/index.html, Accessed 20 Mar. 2025, March 2025.

10. Simmons, B., Geuther, S., and Ahuja, V., "Validation of a Mid-Fidelity Approach for Aircraft Stability and Control Characterization," AIAA AVIATION 2023 Forum, AIAA Paper 2023-4076, June 2023.

11. DiMaggio, G., Simmons, B., Geuther, S., Hartfield, R., and Ahuja, V., "Transition Aero-Propulsive Analysis of a Tilt-Wing eVTOL Aircraft Using a Surface-Vorticity Solver," AIAA SciTech 2025 Forum, AIAA Paper 2025-0654, January 2025.

12. Lawrence, P., Theodore, C., Johnson, W., and Berger, T., "A Handling Qualities Analysis Tool for Rotorcraft Conceptual Designs," *The Aeronautical Journal*, Vol. 122, (1252), 2018, pp. 960–987.

13. Malpica, C., and Withrow-Maser, S., "Handling Qualities Analysis of Blade Pitch and Rotor Speed Controlled eVTOL Quadrotor Concepts for Urban Air Mobility," VFS International Powered Lift Conference, 2020.

14. Withrow-Maser, S., Malpica, C., and Nagami, K., "Multirotor Configuration Trades Informed by Handling Qualities for Urban Air Mobility Application," Proceedings of the Vertical Flight Society's 76th Annual Forum & Technology Display, October 2020.

15. Withrow-Maser, S., Malpica, C., and Nagami, K., "Impact of Handling Qualities on Motor Sizing for Multirotor Aircraft with Urban Air Mobility Missions," Proceedings of the Vertical Flight Society's 77th Annual Forum & Technology Display, May 2021.

16. Schuet, S., Malpica, C., Lombaerts, T., Kaneshige, J., Withrow, S., Hardy, G., and Aires, J., "A Modeling Approach for Handling Qualities and Control Safety Analysis of Electric Air Taxi Vehicles," AIAA AVIATION Forum, June 2020.

17. Malpica, C., Suh, P., and Silva, C., "Flight Dynamics Conceptual Design Exploration of Multirotor eVTOL," Proceedings of the 80th Vertical Flight Society Annual Forum & Technology Display, 2024.

18. Schuet, S., Malpica, C., and Aires, J., "A Gaussian Process Enhancement to Linear Parameter Varying Models," AIAA AVIATION Forum, AIAA Paper 2021-3006, 2021.

19. Altamirano, G. V., Foster, J. V., Malpica, C., and Schuet, S., "Integrated Handling Qualities Safety Analysis for Conceptual Design of Urban Air Mobility Vehicles," AIAA AVIATION 2022 Forum, AIAA Paper 2022-4012, June 2022.

20. Altamirano, G., Matt, J., Foster, J., Suh, P., Hanson, C., Malpica, C., and Schuet, S., "Flying Qualities Analysis and Piloted Simulation Testing of a Lift + Cruise Vehicle with Propulsion Failures in Hover and Low-Speed Conditions," Proceedings of the 79th Annual Forum, May 2023.

21. Malpica, C., Withrow-Maser, S., Aires, J., Schuet, S., Suh, P., Barnes, K., Hanson, C., Ruan, A., Altamirano, G., and Foster, J., "Handling Qualities of Multirotor RPM-Controlled Electric-Vertical Take-Off and Landing (eVTOL) Aircraft for Urban Air Mobility," Proceedings of the Vertical Flight Society's 79th Annual Forum & Technology Display, May 2023.

22. Johnson, W., Silva, C., and Solis, E., "Concept Vehicles for VTOL Air Taxi Operations," AHS Technical Conference on Aeromechanics Design for Transformative Vertical Flight, January 2018.

23. Silva, C., Johnson, W., Antcliff, K. R., and Patterson, M. D., "VTOL Urban Air Mobility Concept Vehicles for Technology Development," Aviation Technology, Integration, and Operations Conference, AIAA AVIATION Forum, AIAA Paper 2018-3847, June 2018.

24. NASA Langley Research Center, "NASA Urban Air Mobility (UAM) Reference Vehicles – "Lift + Cruise"," *Systems Analysis and Concepts Directorate*, 2025, https://sacd.larc.nasa.gov/uam-refs/.

25. Johnson, W., "NDARC – NASA Design and Analysis of Rotorcraft," Technical Report NASA TP-2015-218751, NASA, April 2015.

26. Patterson, M. D., Antcliff, K. R., and Kohlman, L. W., "A Proposed Approach to Studying Urban Air Mobility Missions Including an Initial Exploration of Mission Requirements," , May 2018.

27. The MathWorks Inc., "MATLAB, Version 24.1.0.2653294 (R2024a)," *The MathWorks Inc.*, 2025, https://www.mathworks.com/.

28. Peters, D. A., and HaQuang, N., "Technical Note: Dynamic Inflow for Practical Applications," *Journal of the American Helicopter Society*, Vol. 33, (4), October 1988, pp. 64–68. DOI: 10.4050/JAHS.33.64.

29. Suh, P., Hanlon, P. A., Hunker, K. R., Barnes, K., Fernandez, X. C., Sadey, D. J., Trevino, J., Valco, M. J., Tallerico, T., and Malpica, C., "Real-Time eVTOL Powertrain Modeling for the NASA Vertical Flight Simulator," VFS International 81st Annual Forum & Technology Display, may 19–22, 2025.

30. Wai, J., and Jahns, T. M., "A New Control Technique for Achieving Wide Constant Power Speed Operation with an Interior PM Alternator Machine," IEEE Industry Applications Conference, 36th IAS Annual Meeting, Vol. 2, 2001. DOI: 10.1109/IAS.2001.955545.

31. Krishnan, R., *Electric Motor Drives*, Prentice Hall, Upper Saddle River, 2001.

32. Anon., "Handling Qualities Requirements for Military Rotorcraft," Aeronautical Design Standard-33 (ADS-33E-PRF), U.S. Army Aviation and Missile Command, March 2000.

33. Anon., "Handling Qualities Requirements for Military Rotorcraft," Detail Specification MIL-DTL-32742(AR), Department of Defense, March 2023.

34. Anon., "Aerospace – Flight Control Systems – Design, Installation and Test of Piloted Military Aircraft, General Specification For," SAE-AS94900, July 2007.

35. Durham, W., Bordignon, K., and Beck, R., *Aircraft Control Allocation*, John Wiley & Sons, Chichester, West Sussex, 2017.

36. Boyd, S., and Vandenberghe, L., *Convex Optimization*, Cambridge University Press, 2004, pp. 1–17.

37. Diamond, S., and Boyd, S., "A Python-Embedded Modeling Language for Convex Optimization," *Journal of Machine Learning Research*, Vol. 17, (83), 2016, pp. 1–5.

38. Agrawal, A., Verschueren, R., Diamond, S., and Boyd, S., "A Rewriting System for Convex Optimization Problems," *Journal of Control and Decision*, Vol. 5, (1), 2018, pp. 42–60.

39. Goulart, P. J., and Chen, Y., "Clarabel: An Interior-Point Solver for Conic Programs with Quadratic Objectives," arXiv preprint arXiv:2405.12762, 2024.

40. Lavretsky, E., and Wise, K. A., *Robust and Adaptive Control with Aerospace Applications*, Springer-Verlag, London, first edition, 2013, pp. 51–72.